Quantitative Anisotropy Imaging with Polarized Interference Microscopy

by

Baoliang Ge

Submitted to the Department of Mechanical Engineering
in partial fulfillment of the requirements for the degree of

Master of Science in Mechanical Engineering

at the

MASSACHUSETTS INSTITUTE OF TECHNOLOGY

June 2018

Signature redacted

Author .....
Department of Mechanical Engineering
May 11, 2018

Signature redacted

Certified by .....
Peter T.C. So
Professor
Thesis Supervisor

Signature redacted

Accepted by .....
Rohan Abeyaratne
Chairman, Department Committee on Graduate Theses

Quantitative Anisotropy Imaging with Polarized Interference Microscopy

by

Baoliang Ge

Submitted to the Department of Mechanical Engineering
on May 11, 2018, in partial fulfillment of the
requirements for the degree of
Master of Science in Mechanical Engineering

Abstract

Optical anisotropy measurement is essential for material characterization and biological imaging. Many optical anisotropy imaging techniques have been developed, such as fluorescence polarization microscopy(FPM), liquid crystal based polarization microscopy (LC Polscope), polarization state optical coherence tomography (ps OCT), and polarization Raman spectroscopy. Quantitative phase microscopy (QPM) is another important modality of optical imaging. By implementing interferometry, we can quantitatively map the complex field distribution of the sample with high imaging speed and high throughput. Furthermore, we can use QPM system to reconstruct the three-dimensional structure of the sample by solving inverse scattering problem. My major work is developing high speed, high sensitivity quantitative polarization imaging system. Firstly, I proposed a polarization microscope system for directly imaging sample's retardance distribution by inserting two quarter wave plates between the two crossed linear polarizers in conventional polarization microscopy, before and after the sample. This imaging concept is validated with experimental data of wave plates and liquid crystal retarders. Secondly, I proposed quantitative polarization interference microscopy (QPIM) through designing a compact polarization-resolved interference microscopy system that captures interferograms bearing sample's linear birefringence information. To extract the retardance and the orientation angle maps from a single-shot measurement, we have further developed a mathematical model for QPIM. Our QPIM system has been validated by measuring a calibrated quarter-wave plate, whose fast-axis orientation angle and retardance were determined with great accuracies. We have demonstrated this application by capturing transient retardance changes in a custom-designed parallel-aligned nematic liquid crystal-based device. Finally, I proposed an imaging concept for three-dimensionally reconstruct the polarization distribution for the sample by solving anisotropic Helmholtz equation. All of these three novel imaging techniques have the potential to be applied to the study of sickle cell disease polymerization dynamics, acrosome process of crab sperms, label-free visualization of neuron action potential and semiconductor inspection in the future.

Thesis Supervisor: Peter T.C. So
Title: Professor

Acknowledgments

I appreciate the guide and help from my adviser, Prof. Peter So, who conceive the research project and gave me useful advice based on his profound professional knowledge and experience. I also appreciate Prof. Renjie Zhou in CUHK, who was a postdoc of Laser Biomedical Research Center(LBRC), gave me detailed and comprehensive guidance, including teaching experimental skills and initiating conceptual discussions. I should also give my gratitude to Mr. Yu Tachiguchi in Hamamatsu Corporation, who was also a member in LBRC, prepared the sample of liquid crystal device. Many thanks to prof. Irmgard Bischofberger and her student Qing Zhang from MIT mechanical engineering department for providing me with the orange II fiber samples, and I am also appreciate prof. Matsudaira from Department of biological sciences in NUS for offering the samples of crab sperms. Finally, I should thank to all the members in LBRC and So lab, especially Dr. Poorya Hosseini and Dr. Zahid Yaqoob, for their kind suggestions and substantial help.

Contents

List of Figures

List of Tables

Chapter 1

Introduction

1.1 Motivations

1.1.1 Material Inspection

Optical anisotropy is an intrinsic property of all materials[1, 2]. Liquid crystal (LC) materials are commonly used in research and industry have high optical anisotropy[3]. By measuring the birefringence parameters of LC materials, the performance of LC-based devices can be quantified[4–6]. Recently, the existence of in-plane anisotropy in 2D materials[7], such as black phosphor[8–10] and GaTe[11, 12], has attracted great attention[13, 14]. It has been found that the stress exerted on 2D material[15, 16] and grain boundary[17] can also cause optical anisotropy variations. Furthermore, optical anisotropy property can be used for defect detection on semiconductor wafers[18]. For nanotubes, anisotropic optical scattering has been used for inferring their orientation variations, which can be applied to develop single particle tracking techniques[19].

1.1.2 Biological Imaging

Optical anisotropy is also ubiquitous in biological structures. Polymerized and bundled structures organelles, such as microtubules and actin filaments, have strong birefringent signals that can be observed under polarization sensitive microscopes[20]. Microtubules, actins and other polymerized structures in cells are the fundamental

components for cytoskeletons[21]. They are responsible for many important live activities, such as transmembrane interaction[22], cell migration[23], and actin potential between neurons[24]. Further, polarization sensitive microscopes have many medical applications. For example, collagen is a highly anisotropic biological material that is a main component of biological tissues[25] and polarization sensitive microscopes may reveal pathological change of collagen structures in muscles, eye and skin[26].

1.2 Optical Anisotropy Imaging Techniques

1.2.1 Fluorescence Polarization Microscopy

Fluorescence microscopy is widely used in biological researches[27]. Fluorophores, such as green fluorescent proteins(GFPs), emit light as dipoles. This means that the fluorescence is highly polarized, with most of its energy polarized along the dipole's axis[28]. If the fluorophores are tightly labeled to anisotropic biological structures such as actins, microtubules and other polymers, they will orient along with the polymers they bound to. Therefore, if we use a polarization sensitive system to collect the fluorescence, we will be able to observe the orientation and accumulation of the actins or microtubules, even if their geometric size is below the diffraction limit of the microscope. Researchers use this technique, called fluorescence polarization microscopy (FPM)[29], to observe the structures and dynamics of chromosomes, lipid bilayers, and the cytoskeleton in live cells. If FPM is combined with total internal refraction fluorescence microscopy(TIRFM), researchers can even track the position and orientation of a single molecule three dimensionally and simultaneously[28]. C. Cruza et.al. proposed a polarized super-resolution microscopy by combing the fluorescence polarization microscopy and super-resolution microscopy[29, 30]. This technique enables us to observe the live cell filaments and DNAs' orientation and architecture in nanoscale.

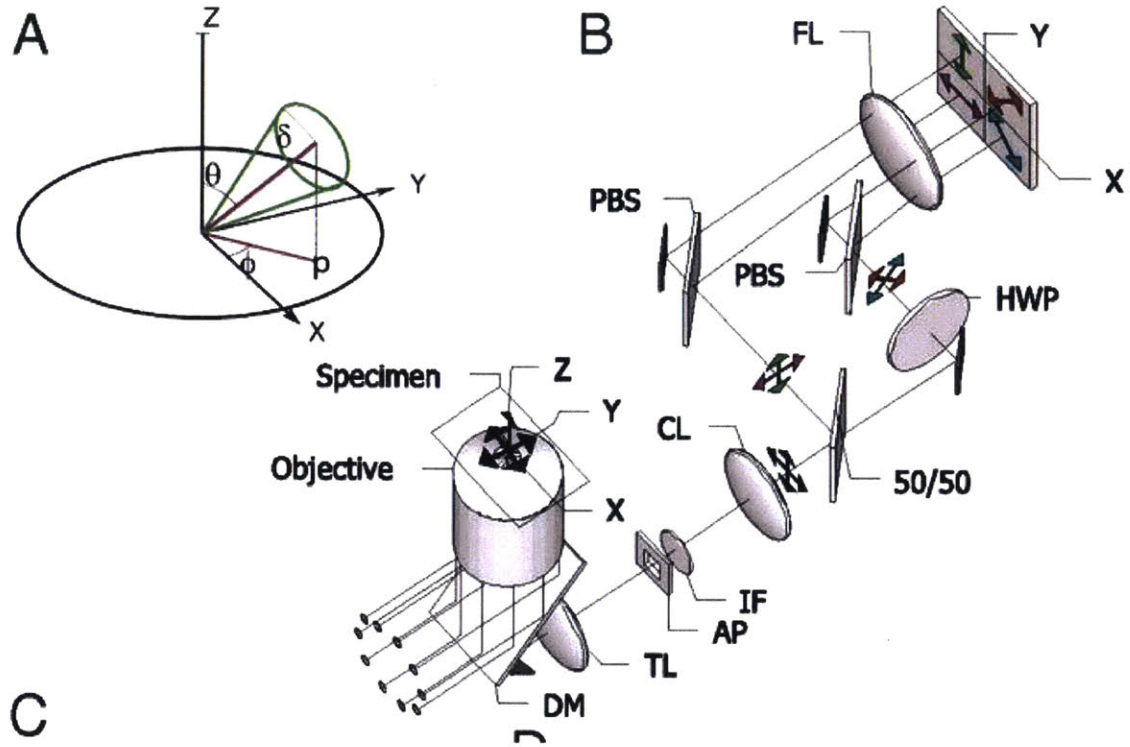

Figure 1-1: A. The angular distribution of dipoles; B. Schematic of the microscope. AP, aperture; CL, collimating lens; DM, dichroic mirror; IF, interference filter; PBS, polarization beam splitter; TL, tube lens.

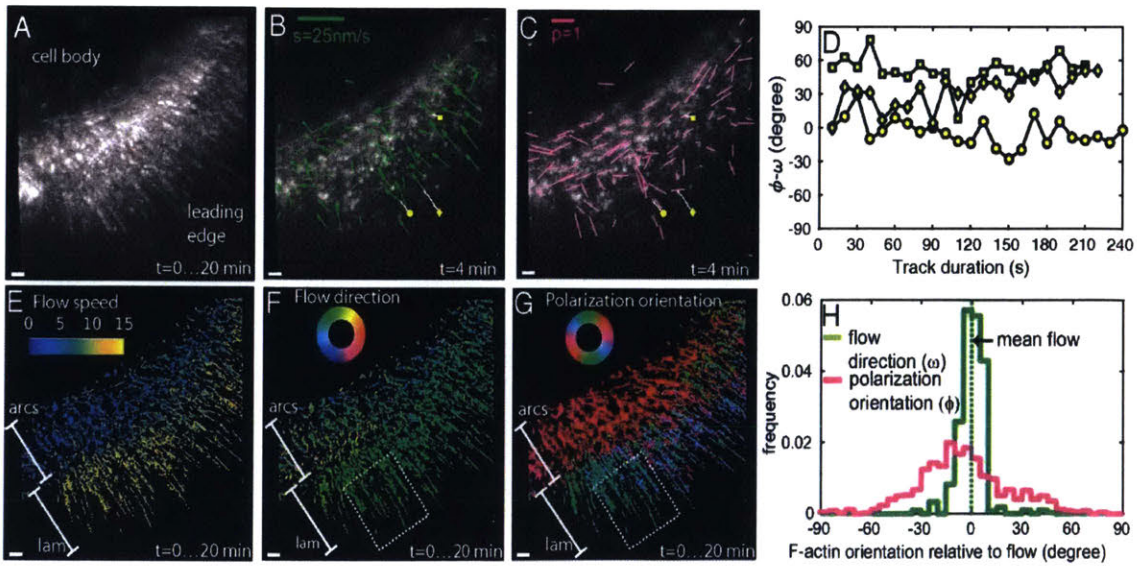

Figure 1-2: Position and orientation of AF488-phalloidin bound to F-actin during retrograde flow in live cells. (Detailed caption can be found in ref.[28]).

1.2.2 Liquid Crystal Based Polarization Microscopy (LC Pol-scope)

Birefringence is also an intrinsic marker for anisotropic biological fine structures, which can be revealed by polarization microscopes without any labeling[1]. However, it is challenging for conventional polarization microscopes to quantify the retardance and orientation angle distributions[31, 32]. By replacing the polarization compensators with LC-based variable retarders in conventional Pol-scopes, Oldenbourg and co-workers quantified the two-dimensional (2D) distributions of birefringence parameters[33–35]. The general universal liquid crystal retarders which are used in the LC pol-scope's system design (shown in Figure 1.3) can change the polarization state of the illumination light. With a self-developed algorithm, Oldenbourg and co-workers can retrieve the 2D retardance and orientation angle distribution with high accuracy and sensitivity.

As a quantitative polarization imaging method, LC Pol-scope is able to image and quantify many biological processes, such as cell mitosis, cell migration and polymerization[36]. With high imaging sensitivity and spatial resolution, LC -scope can quantify the image information to the level of single microtubules[37], as shown in Figure 1.4.

1.2.3 Polarization-state Optical Coherence Tomography(PS-OCT)

Optical Coherence Tomography (OCT) has been established for almost 25 years as a successful imaging technique for high-resolution cross-sectional and three-dimensional imaging of transparent biological tissues[38]. It has been widely applied in medical imaging for ophthalmology diagnosis[39, 40] and blood flow detection[41, 42]. However, OCT mostly provides the morphology information but does not provide tissue-specific contrast complicating image interpretation. Polarization state optical coherence tomography(PS-OCT)[42, 43] can reveal the anisotropic structure in biological tissues, and provides additional information for medical diagnosis[44].

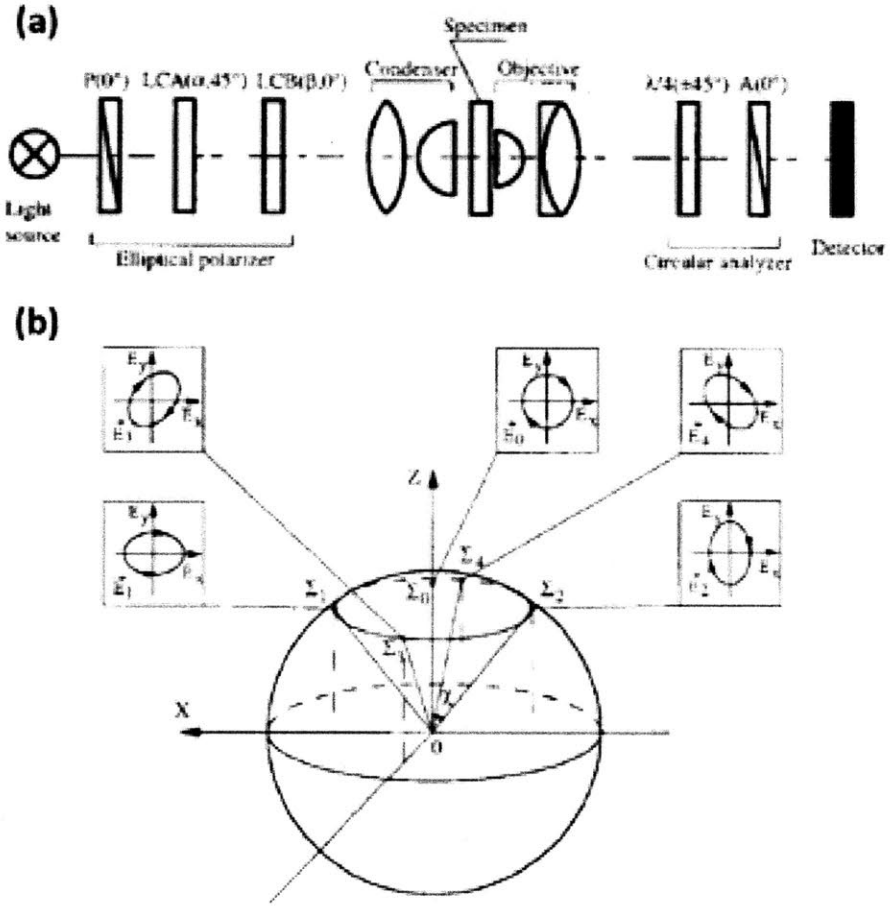

Figure 1-3: (a) Schematics of the polarized light microscope with a liquid crystal universal compensator in the illumination path. (b) Settings of the probe beam on the Poincare sphere. Σ_0 is the setting with right-circular polarization; $\Sigma_1, \Sigma_2, \Sigma_3$ and $\Sigma_4$are settings with elliptical polarizations.

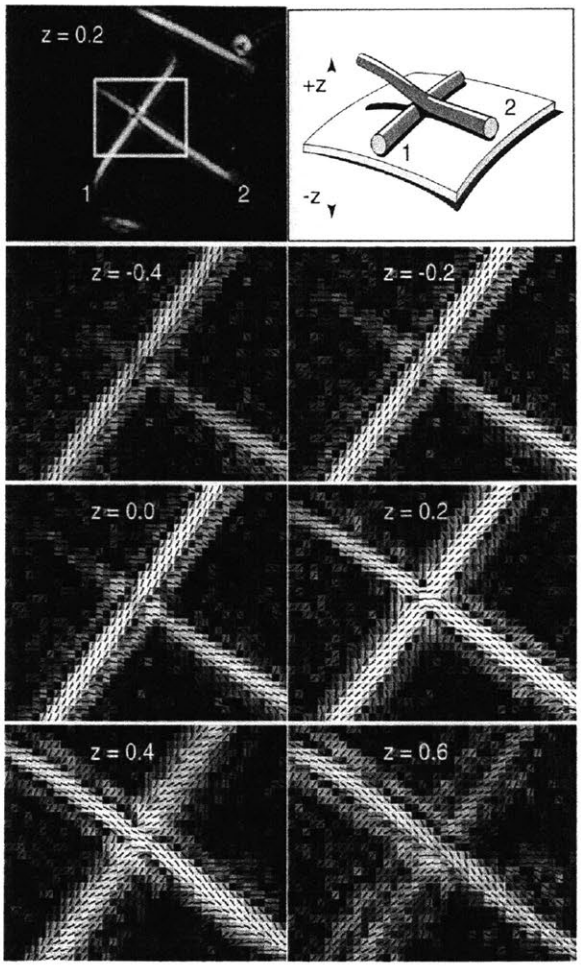

Figure 1-4: Top left image shows two axonemes that cross each other while adhering partly to the cover glass. The top right drawing depicts the arrangement of the two axonemes as derived from the focus series shown in the images below. The focus level of each image is given as a z value in m (z = 0 for focus at cover glass surface, positive z for focus positioned in aqueous medium with axonemes, negative z for focus positioned inside cover glass)

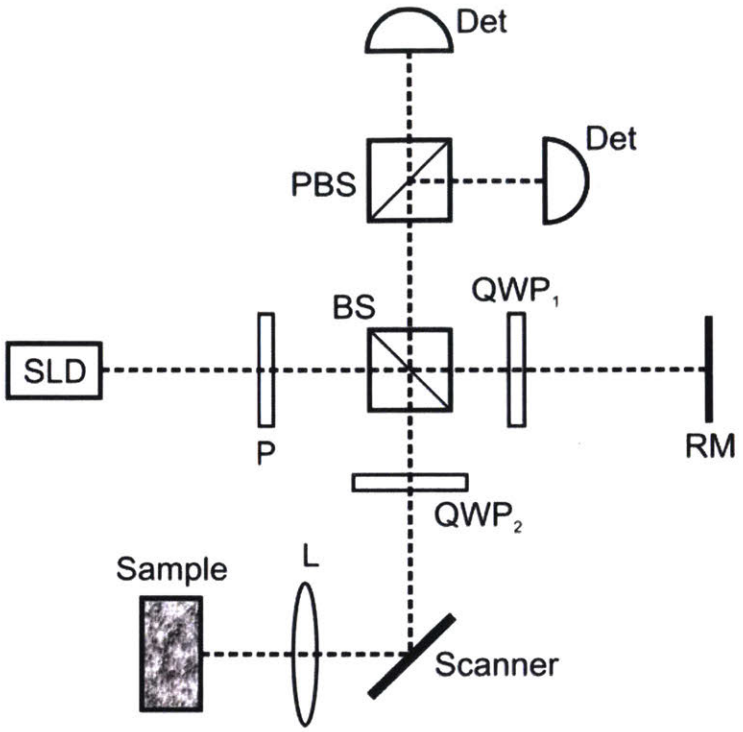

Figure 1-5: Sketch of basic PS-OCT system. BS, beam splitter; Det, detector; P, polarizer; PBS, polarizing beam splitter; QWP, quarter wave plate; RM, reference mirror; SLD, super luminescent diode.

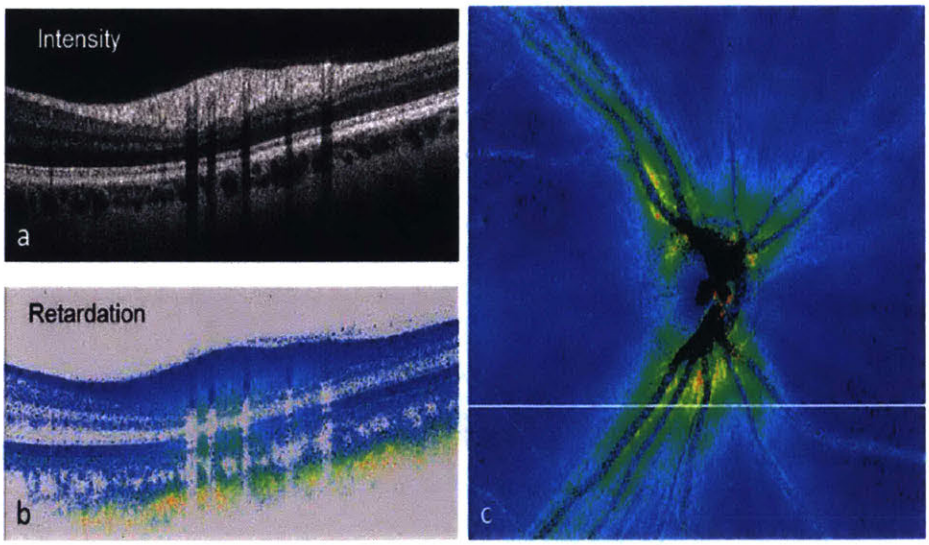

Figure 1-6: PS-OCT images recorded in the optic nerve head region of a healthy human eye. (a) Reflectivity B-scan; (b) retardation B-scan; (c) en-face RNFL retardation map. The white line indicates the position of the B-scans.

1.2.4 Polarized Raman Spectroscopy

With the fast development of material science, the characterization of the material's physical properties becomes more important. Raman spectroscopy is a widely used technique of material characterization since it is capable of revealing sample's chemical information[45]. Recently, the anisotropy in 2D material and other novel materials have attracted attention from many researchers[13–16]. Polarized Raman spectroscopy is developed and applied in the characterization of these anisotropic materials[46]. By inserting a linear polarizer and a half wave plate in the illumination part of the Raman spectroscopy, the researchers are able to illuminate the sample with linear polarized light and adjust its orientation of oscillation. The collected Raman scattering spectrum under different polarization orientations will reveal the material's anisotropic information. One example of the material characterization with polarized Raman spectroscopy is shown in Figure 1.7.

1.3 Complex Field Imaging and Tomography

Polarization microscopy is a well-developed area and many techniques have been developed to be applied in optical anisotropy imaging. However, the quantitative polarization imaging still requires multiple measurements[33–35] or the split of camera's frame[28, 47]. This limitation restricts the imaging speed and the field-of-view of quantitative polarization microscopes. One solution for this limitation is to combine polarization imaging with quantitative phase microscopy(QPM)[48]. Since we have two unknowns for the polarization imaging, i.e., retardance and orientation angle, it is impossible to retrieve them both with a single image of intensity distribution. However, QPM is able to retrieve the complex field distribution of the sample in a single shot, which means we can obtain the information of amplitude and phase simultaneously[49–53]. This advantage of QPM provides the possibility of single-frame quantitative polarization imaging. In this part, I will introduce several popular quantitative phase imaging techniques. Another challenge for quantitative polarization microscopy is to realize three-dimensional quantitative polarization mapping

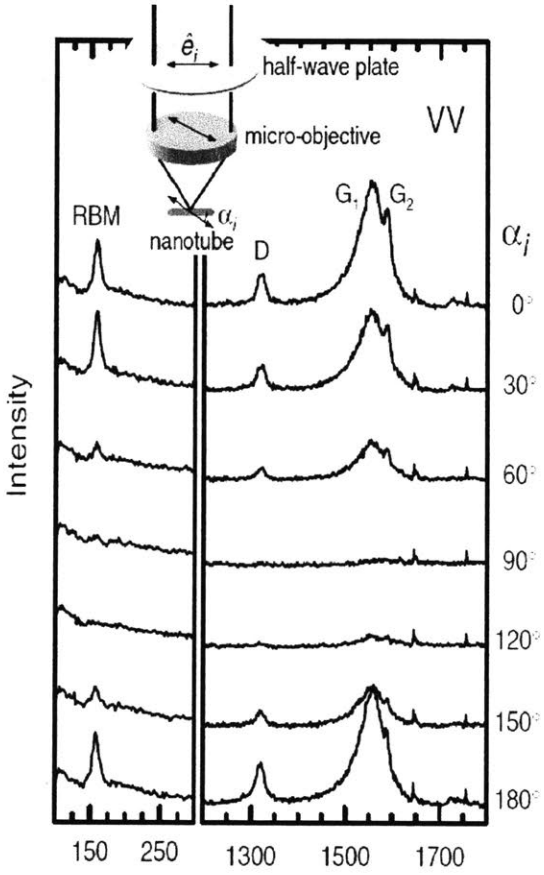

Figure 1-7: Raman spectra of a thin SWNT rope in the VV configuration for various angles α_i between the rope axis and the polarization of the incident laser beam, as depicted in the inset.

with a wide-field microscopy setup. Recently, optical diffraction tomography (ODT) has been shown to be a promising method for fast volumetric optical imaging[54–58]. This technique is based on complex field imaging, and we can reconstruction 3D image by angle-scanning, temporal or spatial gating. In this part, I will introduce angle-scanning optical diffraction tomography and white light tomography[59]. In the following chapters, I will propose a possible method to realize 3D polarization mapping with optical diffraction tomography.

1.3.1 Off-axis quantitative phase microscopy(QPM)

Phase-contrast microscopes have been widely used in biological imaging[60]. By inserting a phase plate in the back focal plane (BFP), a phase shift has been introduced between the unscattered light and scattered light, and the interference of them visualizes the transparent tissue inside biological samples. However, the images captured by phase-contrast microscopy are qualitative. To quantitatively retrieve the phase information, one efficient method is to introduce a reference beam in an optical microscope system. The reference beam is horizontally shifted an angle to the optical axis, which is called off-axis interferometry. This technique is generally called digital holography microscopy(DHM)[61–63]. From the hologram captured on the camera, we can quantitatively retrieve the amplitude and phase of the sample. The standard system design of DHM is shown in Figure 1.8.

The phase delay of the sample $\phi(x, y)$ can be expressed as:

$$\phi(x, y) = \frac{2\pi}{\lambda} \int_0^{h(x,y)} [n(x, y, z) - n_0] dz \tag{1.1}$$

where $n(x, y, z)$ is the refraction index of the sample at the position (x, y, z),n_0 is the refraction index of the medium.$h(x, y)$is the thickness of the sample at the position (x, y).If the angle between the reference beam and the optical axis is α, we can express the intensity on the camera as:

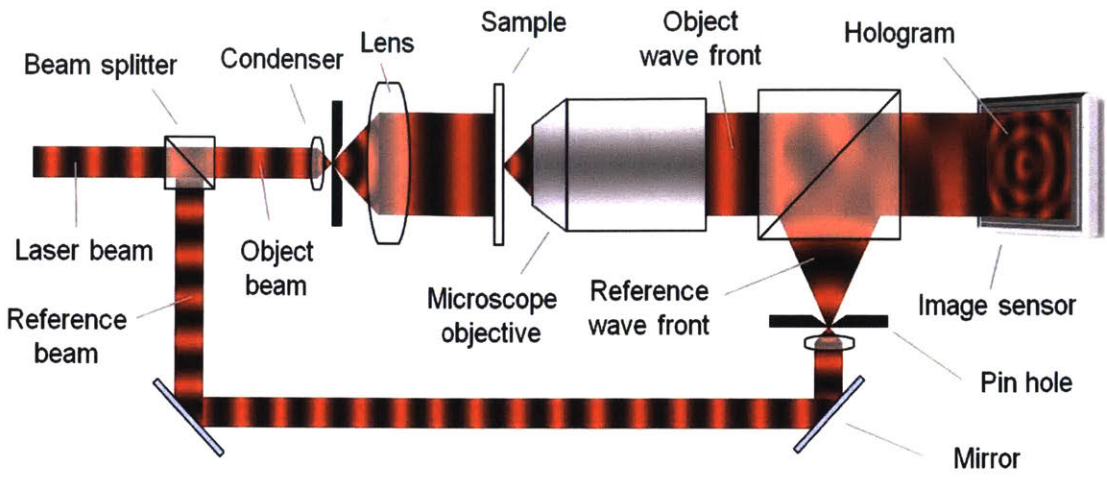

Figure 1-8: Typical optical setup for digital holography microscopy(DHM).

$$I(x,y) = |U_0|^2 + |U_1(x,y)|^2 + 2|U_0||U_1(x,y)|cos[\Delta\phi(x,y) + kxsin\alpha], \tag{1.2}$$

where $k = 2\pi/\lambda$ and λ is the wavelength of the illumination light. By performing Fourier transform[64] and unwrap algorithm[65], we can retrieve the phase distribution of the sample.

However, there are some disadvantages of the DHM systems. Firstly, since the scattered beam and reference beam should be coherent with each other, it requires a light source with very long coherence length. This will introduce speckles in the images and degrade their quality. Secondly, the reference beam and the scattered beam are not common-path. The mechanical vibration and air fluctuation will introduce noise in the phase measurement. To overcome these disadvantages, diffraction phase microscopy (DPM)[66–70] has been developed. In DPM, the light scattered by the sample comes out of the microscope and separated by a diffraction grating. Then a 4f system is used to relay the optical system. On the Fourier plane of the 4f system, we let the 0^{th} order pass and use a pinhole to filter the 1^{st} order. The 1^{st} order becomes the reference beam, and the interferogram is recorded on the camera which

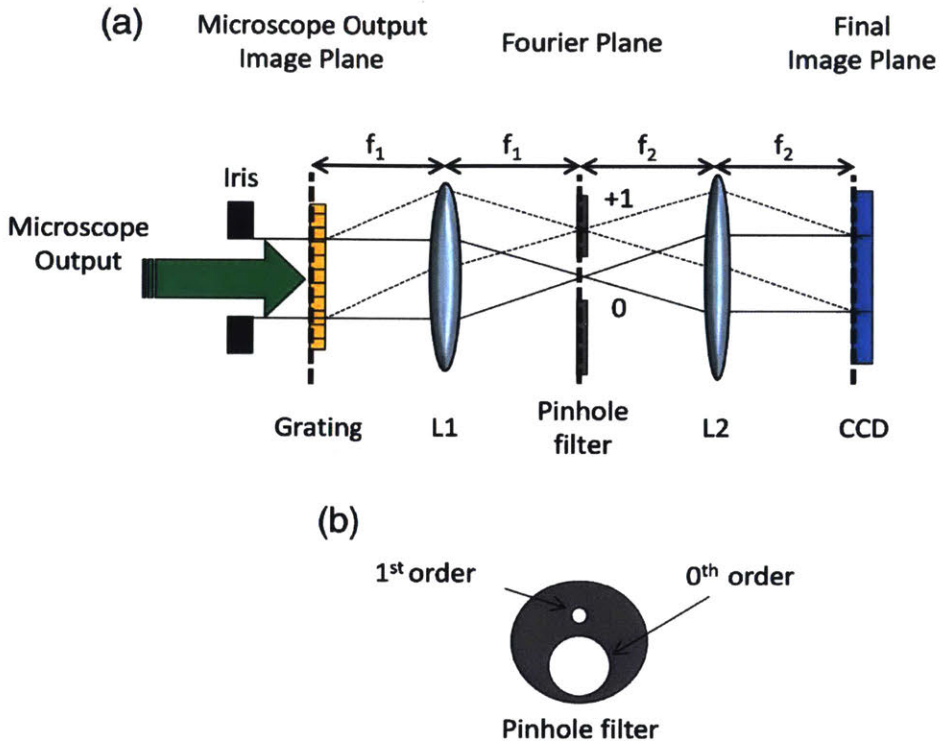

Figure 1-9: (a) Typical optical setup for diffraction phase microscopy(DPM). (b) the scheme diagram of the pinhole filter.

is put on the image plane. In this way, the scattered beam and the reference beam are near-common-path. The influence of mechanical vibration and air fluctuation is minimized. Therefore, DPM has extremely high sensitivity of phase measurement. Since the optical path difference of the two beams is small (shorter than a wavelength), we can use low coherent light source, such as white light, LED or super-continuous laser. The image has less speckle and the image quality is significantly improved. Recently, DPM has been used in the observation of membrane fluctuation of red blood cells (RBCs) and the temperature distribution measurement in the liquid.

1.3.2 Spatial light interference microscopy(SLIM)

Even if the off-axis interferometric microscopy can provide with a quantitative complex field map of biological samples, its applications have been largely restricted to red blood cell imaging, measuring cell dry mass and imaging other structures with high

uniformity. There are several reasons for these limitations. Firstly, in off-axis QPM, the light source usually has high coherence. The speckles generated by the laser will degrade the spatial sensitivity and contrast. Even if we can use white light for DPM, the contrast of the fringes is low which will cause reduce phase measurement sensitivity. Secondly, the complexity of off-axis QPM system is usually high and requires frequent maintenances. To overcome these restrictions, spatial light interference microscopy(SLIM) is presented by G. Popescu et.al. as a high sensitivity quantitative phase imaging method[71–73]. Instead of shifting the phase of the unscattered light with a phase ring in conventional phase-contrast microscopes, SLIM delays the phase by a liquid crystal phase modulator(LCPM) on the Fourier plane. For a spatial coherent imaging system, after passing the specimen, the portion remains unscattered forms a uniform background of the image; the other portion is scattered and contains the fine structure information of the specimen. Therefore, the intensity on the CCD can be expressed as:

$$I(x,y;\varphi) = |U_0|^2 + |U_1(x,y)|^2 + 2|U_0||U_1(x,y)|cos[\Delta\phi(x,y) + \varphi], \tag{1.3}$$

where U_0 is is the unscattered light and $U_1(x,y)$ is the scattered light of the sample, $\Delta\phi(x,y)$ is the phase difference between U_0 and $U_1(x,y)$, and φ is the phase modulated by the LCPM. The quantity of $\Delta\phi(x,y)$ can be retrieved as:

$$\Delta\phi(x,y) = tan^{-1}[\frac{I(x,y;-\pi/2) - I(x,y;\pi/2)}{I(x,y;0) - I(x,y;\pi)}] \tag{1.4}$$

Because of the extremely short coherence length of this illumination light, approximately 1.2 μm, SLIM provides speckle-free imaging with sub-nanometer spatial background noise. However, since we need multiple measurements for the imaging, the imaging speed of SLIM may be slower than off-axis QPM systems.

1.3.3 Angle scanning optical diffraction tomography (ODT)

Volumetric imaging is another interesting topic in optical imaging. To quantitatively retrieve the three-dimensional refraction index distribution of the sample, W. Choi

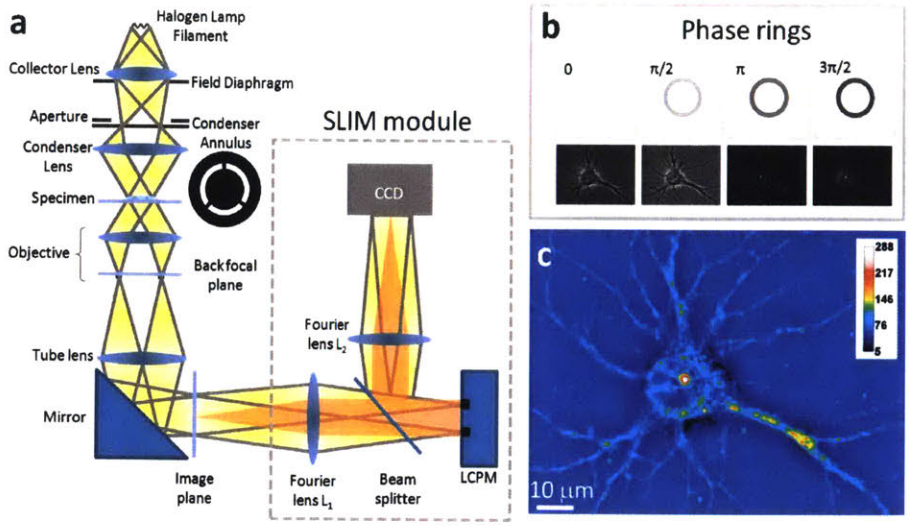

Figure 1-10: SLIM principle. (a) Schematic setup for SLIM. (b) The phase rings and their corresponding images recorded by the CCD. (c) SLIM quantitative phase image of a hippocampal neuron.

et.al. proposed tomographic phase microscopy(TPM) based on measurement of projections of refractive index in multiple directions, in analogy to computed X-ray tomography, in which the projection of absorption is measured[54]. For high resolution live cell imaging, Y. Sung et.al. improved the algorithm of TPM by taking the optical diffraction into account and proposed optical diffraction tomography(ODT)[55]. The system design for TPM and ODT is shown in figure 1.11, which is based on Mach Zehnder interferometry and utilized a galvo scanner to adjust the illumination angle[74]. The 3D reconstruction algorithm is established based on solving an inverse scattering problem. For the optical field in the medium, the homogeneous Helmholtz equation applies:

$$\bigtriangledown^2 U_i(\vec{r}) + n_m^2 \beta^2 U_i(\vec{r}) = 0 \tag{1.5}$$

where $U_i(\vec{r})$ is the illumination light field, and n_m is the illumination light field, and β is the wave number, which is equal to $2\pi/\lambda$, and λ is the wavelength of the illumination light. In the sample, the heterogenous Helmholtz equation is valid:

$$\nabla^2 U(\vec{r}) + n^2\beta^2 U(\vec{r}) = 0 \tag{1.6}$$

where $U(\vec{r}) = U_i(\vec{r}) + U_s(\vec{r})$. $U_s(\vec{r})$ is the scattering field, and $U(\vec{r})$ is the total field to be measured. Under Born approximation, we can assume $U_s(\vec{r}) << U_i(\vec{r})$. We define the scattering potential of the sample to be $\chi(\vec{r}) = n^2(\vec{r}) - n_m^2$, and the wave vector of the illumination light is $\vec{k_i} = (k_{ix}, k_{iy}, k_{iz})$.We can obtain the governing equation for this scattering problem:

$$\nabla^2 U_s(\vec{r}) + n_m^2\beta^2 U_s(\vec{r}) = -\beta^2\chi(\vec{r})exp(i(k_x x + k_y y + k_z z)), \tag{1.7}$$

Through vector space method or a Green's function approach, the scattered field is solved in the transverse Fourier space for a particular focal plane z (is $z = 0$ the imaging plane) as:

$$U_s(k_x, k_y; z) = \frac{e^{\pm qz}}{q}\chi(k_x - k_{ix}, k_y - k_{iy}, \pm q - k_{iz}), \tag{1.8}$$

where $q = \sqrt{\beta^2 - k_x^2 - k_y^2}$. Therefore, The inverse scattering solution to the object function is therefore given by:

$$\chi(k_x - k_{ix}, k_y - k_{iy}, \pm q - k_{iz})) = \frac{q}{e^{\pm qz}}U_s(k_x, k_y; z). \tag{1.9}$$

1.3.4 White light diffraction tomography (WDT)

In angle-scanning optical diffraction tomography, the light source is highly coherent. Therefore, the 3D reconstruction is performed with Fourier space mapping. With incoherent illumination, one can selectively image different sample depths through creating an optical sectioning effect, i.e., achieving coherence-gated ODT[74]. If we use broad-band light source, i.e. white light illumination, we can obtain optical sectioning with temporal gating, which is called white-light diffraction tomography(WDT)[59]. In interferometric imaging, the measurement is the cross-correlation function between the scattered field, Us , and the reference field, Ur. The temporal cross-correlation

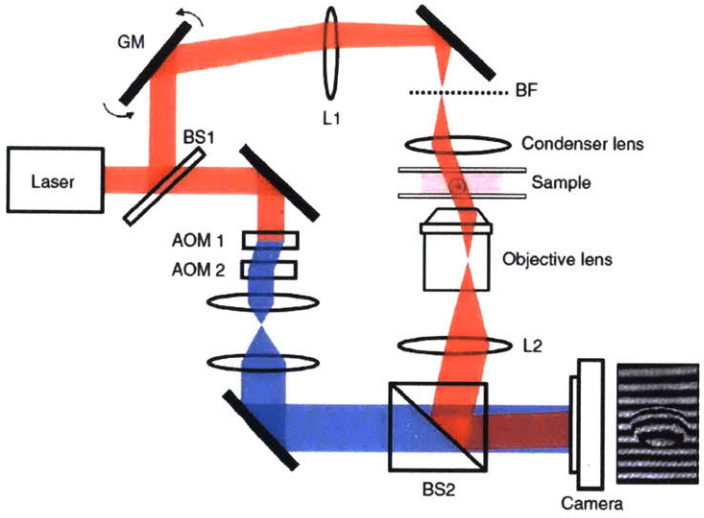

Figure 1-11: Tomographic phase microscope. BS1 and BS2, beamsplitters 1 and 2; GM, galvanometer scanning mirror; L1, focal length f = 250-mm lens; BF, back focal plane of condenser lens; L2, f = 200-mm lens. The sample laser beam with original laser frequency is shown in red, and the frequency-shifted reference laser beam is shown in blue. A typical fringe pattern for a tilted beam illuminating a single HeLa cell is shown.

function can be given by:

$$\Gamma_{12}(\vec{r},\tau) = \langle U_s(\vec{r},t)U_r^*(\vec{r},t+\tau)\rangle_t, \tag{1.10}$$

where τ is the temporal delay. We can relate Γ_{12} to the cross-spectral density function $W_{12}(\vec{r},\omega)$ through a Fourier transform,

$$\Gamma_{12}(\vec{r},\tau) = \int_0^\infty W_{12}(\vec{r},\omega)e^{i\omega t}d\omega, \tag{1.11}$$

where $W_{12}(\vec{r},\omega) = \langle U_s(\vec{r},\omega)U_r^*(\vec{r},\omega)\rangle$. For the WDT, using the forward scattering field solution, the scattering potential can be reconstructed with:

$$\chi(U,V,W) = \frac{\Gamma_{12}(U,V,W)}{\Sigma(U,V,W)}. \tag{1.12}$$

where $U = k_x$, $V = k_y$. $W = q - \beta = \sqrt{\beta^2 - k_x^2 - k_y^2} - \beta$, and$\Sigma(U,V,W)$ is the 3D coherent transfer function which is given by:

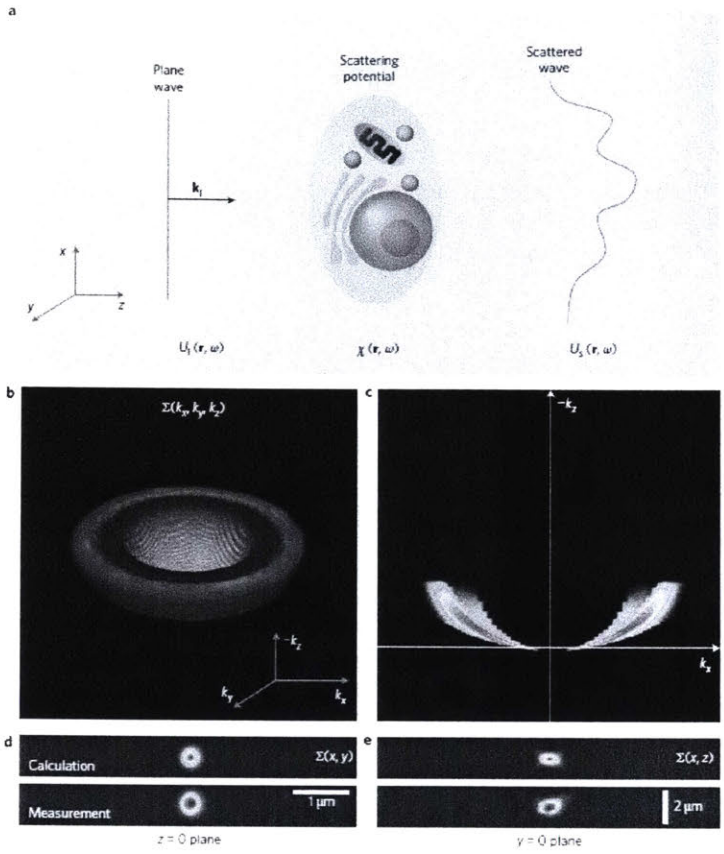

Figure 1-12: The scattering problem. a, Illustration of light scattering under the first-order Born approximation where a plane wave's wavefront is perturbed by the object. b, Three-dimensional rendering of the instrument transfer function, using the proposed WDT calculation. c, Cross-section of the transfer function at the plane. d, Calculated and measured PSF at the $y = 0$ plane. e, Calculated and measured PSF in the $y = 0$ plane

$$\Sigma(U, V, W) = [(W^2 + k_\perp^2)^2 / W^3] S[-(W^2 + k_\perp^2)/2W]. \tag{1.12}$$

which is determined by the light source spectrum S and the numerical aperture (NA) of the imaging system.

Chapter 2

High-sensitivity Retardance Imaging

Retardance is defined by the phase difference between the extraordinary and the ordinary axes of birefringent samples. The magnitude of retardance indicates the extent of accumulation of microtubules, actin filaments or other polymers in biological imaging. Conventional polarization microscope utilizes crossed linear polarizers to image birefringent samples. The intensity of image will change with the rotation of birefringent sample's orientation, which means we cannot obtain the map of retardance with a single measurement. In this chapter, I proposed a simple and efficient method to directly image the retardance distribution of birefringent sample. Two quarter wave plates are inserted between the two crossed linear polarizers in conventional polarization microscopy, before and after the sample. If the sample is weakly anisotropic, the intensity will be proportional to the square of retardance. Moreover, if some proper phase retrieval method is applied, we can also extract the information of orientation angle.

2.1 System Design

The experiment setup used for high sensitivity retardance imaging is shown in Figure 2.1. We used a super-continuous laser and picked a wavelength of 633nm with an Acousto-optical tunable filter. The bandwidth of the illumination light source is 8nm, which can efficiently reduce the spatial coherence and improve the image quality.

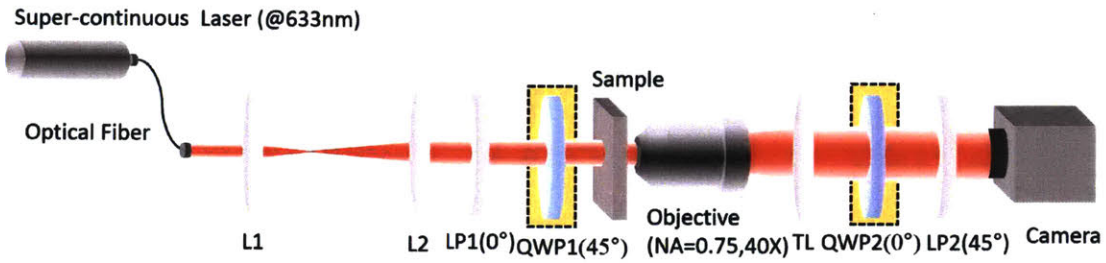

Figure 2-1: System design for high-sensitivity retardance imaging. L1, L2, lens for expanding the laser beam; LP1, LP2, linear polarizers; QWP1, QWP2, quarter wave plates; TL, tube lens.

The laser is coupled into a single-mode fiber for 633nm, and then collimated and expanded by a 4f system. Then we let the laser beam transmits through a linear polarizer(LP1) and a quarter wave plate(QWP1). The angle between the orientation of linear polarizer's axis and quarter wave plate's fast axis is set to 45 degrees, in order to generate circular polarization illumination on the sample. After the light transmits through the sample, it is collected by an objective, and imaged by a tube lens whose focal length is 200mm. Before the image plane, we put another quarter wave plate(QWP2) to 're-linearize' the polarization sate. Here, 're-linearize' means that if there is no birefringent signal, we use this QWP to turn the circular polarization into linear polarization again. The orientation of the linear polarized light is 45 degrees to the fast axis of the QWP. We used another linear polarizer (LP2) to cancel the background signal by setting its orientation direction orthogonal to the re-linearized light. Then the image with its intensity only related to the sample's retardance is recorded by a camera (Pointgrey, FL3-U3-13Y3M-C; full frame 1024×1280 pixels; pixel size $4.8\mu m \times 4.8\mu m$) on image plane. The detailed theoretical analysis will be demonstrated in the next section.

2.2 Theories

In this part, I will use Jones Matrix calculus to demonstrate our idea that our proposed system is able to directly image the birefringent sample's retardance distribution without multiple measurements. Also, this can also be used as the theoretical basis for developing the quantitative imaging. Firstly, we utilized the right-handed circular polarized light to illuminate on the sample, which can be expressed by Jones vector as:

$$\vec{E}_{in} = \frac{1}{\sqrt{2}} \begin{bmatrix} 1 \\ i \end{bmatrix}, \tag{2.1}$$

Then we can describe the Jones matrix of anisotropic sample we are about to image by:

$$J_{sample} = \begin{bmatrix} cos\varphi & -sin\varphi \\ sin\varphi & cos\varphi \end{bmatrix} \begin{bmatrix} e^{i\phi_e} & 0 \\ 0 & e^{i\phi_o} \end{bmatrix} \begin{bmatrix} cos\varphi & sin\varphi \\ -sin\varphi & cos\varphi \end{bmatrix}, \tag{2.2}$$

where ϕ_e and ϕ_o are phase delay of the light field on the extraordinary axis and ordinary axis of the anisotropic sample. The difference between them ($\Delta = \phi_e - \phi_o$)is the retardance distribution we want to image.φ denotes the angle between the extraordinary axis and the x-axis we defined, which we called 'orientation angle'. All of these parameters are varied spatially throughout the sample, but we dropped the spatial coordinates (x, y) in the formula to make the expressions concise. Therefore, with Jones calculus, we can calculate the Jones vector of the output field as:

$$\vec{E}_{out} = J_{LP(45°)} J_{QWP} J_{Sample} E_{in} = \frac{e^{-i\pi/4}}{2\sqrt{2}} \begin{bmatrix} (e^{i\phi_e} - e^{i\phi_o})(cos2\varphi - isin2\varphi) \\ ... \end{bmatrix}, \tag{2.3}$$

The output complex field on the image plane is:

$$E_{out} = \frac{e^{-i\pi/4}}{2\sqrt{2}} (e^{i\phi_e} - e^{i\phi_o})(cos2\varphi - isin2\varphi), \tag{2.4}$$

Here E_{out} is also a function of (x, y). The measured intensity on the camera can be expressed as:

$$I_{out} = \frac{1}{8}(e^{i\phi_e} - e^{i\phi_o})(cos2\varphi - isin2\varphi)(e^{-i\phi_e} - e^{-i\phi_o})(cos2\varphi + isin2\varphi) = \frac{sin^2\Delta}{2}, \quad (2.5)$$

Therefore, the image we obtained on the image plane is only related to the retardance, which means we can directly retrieve the retardance without rotating the polarizers or doing multiple measurements. Furthermore, if we assume the scatter of the sample is weak, which means the phase delay is small:

$$e^{i\phi_e} \simeq 1 + i\phi_e, e^{i\phi_o} \simeq 1 + i\phi_o, \quad (2.6)$$

The output field can be simplified to:

$$E_{out} \simeq \frac{\Delta}{2\sqrt{2}} exp(i(\frac{\pi}{4} - 2\varphi)). \quad (2.7)$$

We can quantitatively obtain the retardance and orientation angle by retrieving the amplitude and phase of the complex field. This means that we can do single-shot quantitative polarization imaging by applying phase retrieval techniques in polarization microscopes. This will be an important direction for this project in the future.

2.3 Calibration

2.3.1 Wave Plate

Based on our theory demonstrated in the last section, the recorded intensity should not be changed when we rotate the sample, since the intensity is only related to the retardance. To validate this imaging concept, we imaged the half wave plate at 808nm (WPH10M-808, Thorlabs) when we rotate its fast axis from 0 to 360 degrees. We took one full frame image for each 10-degree increment and calculated its average value. We normalized these calculated average values with the saturation intensity of the camera

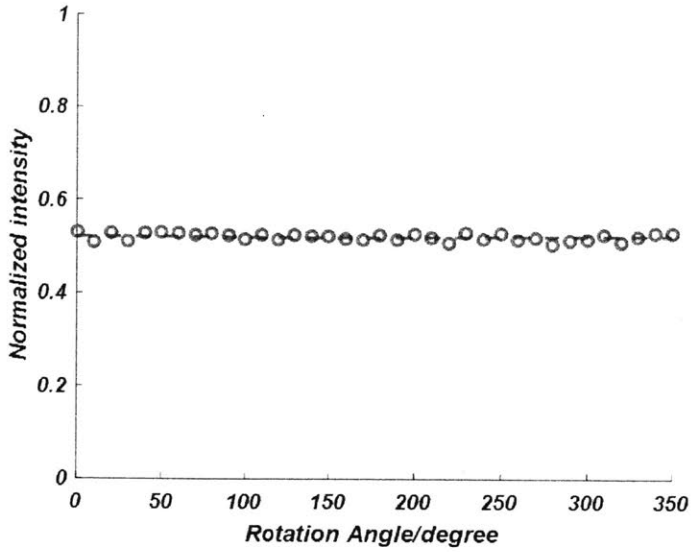

Figure 2-2: the averaged normalized intensity as a function of rotation angle of a zeroth order half wave plate @ 808nm. The red spots depict the measured data; the blue dashed line shows the mean value of the normalized intensity.

(determined by the well depth of the camera and the integration time). In figure 2.2, the normalized average intensities as a function of rotation angle is plotted. From this measurement, the normalized intensity is (0.5213± 0.0074), which means the fluctuation of the intensity is only 1.42% of the measured normalized intensity. This subtle error may come from the spatial variance difference on the different region of the wave plate, or the slightly impurity of the circular polarized illumination. Anyway, we can say our method can decouple retardance and orientation angle and directly image the retardance distribution of birefringent samples.

2.3.2 Variable Liquid Crystal Retarder

However, even if we can directly image the retardance distribution, the measurement is qualitative and we cannot know the absolute retardance value. Therefore, in order to quantitatively image the retardance, we use a variable liquid crystal retarder (LCC1411-A, Thorlabs) as the sample to calibrate the relation between the sample's retardance and recorded intensity. The retardance of the liquid crystal retarder will be changed as a function of the applied voltage. The relation of retardance and

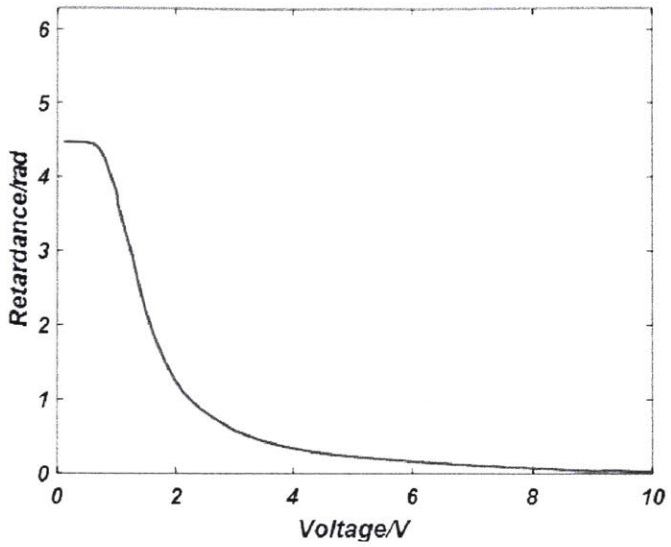

Figure 2-3: the retardance as a function of applied voltage. The voltage value is the root mean square of the applied source.

applied voltage is shown in Figure 2.3, which is provided by the manufacturer.

Then we measured the normalized intensity when we image the liquid crystal retarder as the calibration of the retardance. The voltage source is a zero-centered rectangular voltage wave is applied through a function generator (DS345, Stanford Research Systems). The recorded intensity will be also influenced by the power of the input laser source and the integration time of the camera. Therefore, we measured the normalized average intensity of the full frame as a function of the applied voltage under different input laser power (53 μW, 113 μW, 336 μW, 833 μW) and integration time (5ms, 10ms, 20ms, 30ms, 100ms). The corresponding plot is shown in Figure 2.4.

We can numerically fit the curves depicted in Figure 2.3 and 2.4 to calibrate the relation of the intensity and retardance. However, the background of the recorded intensity is a little bit high due to the impurity of the polarized light and the read noise of camera. Some of the intensities are saturated because the well depth of the camera is limited (N = 10651).

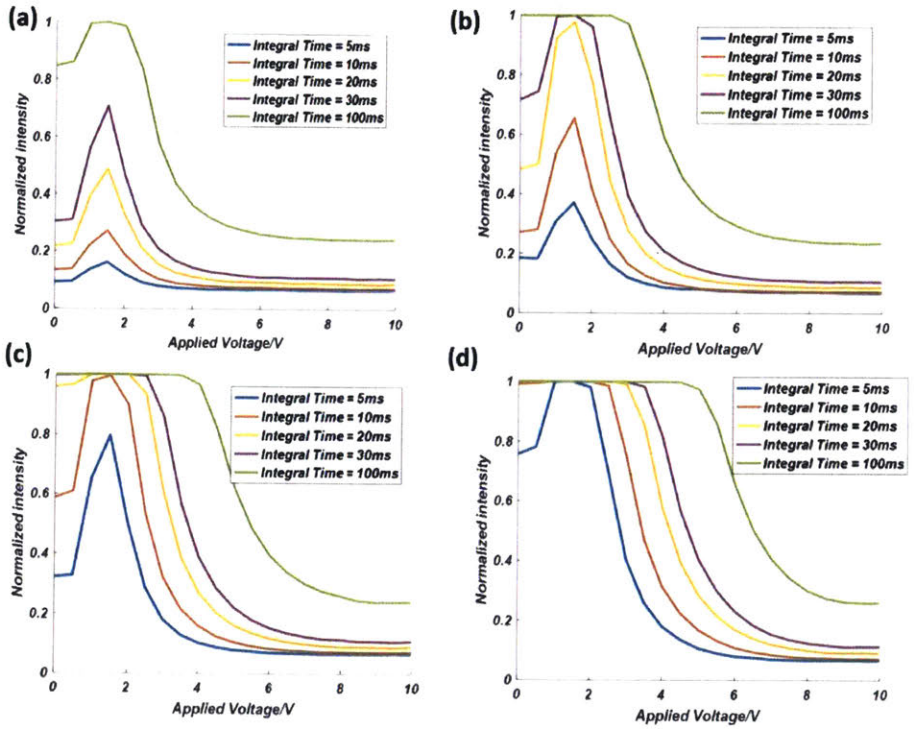

Figure 2-4: the normalized average intensity as a function of applied voltage under different input laser power (a) 53 μW; (b) 113 μW; (c)336 μW; (d) 833 μW. In each subfigure, the curves plotted in different camera integration times are denoted with different color. The increment of the applied voltage is 0.5V. The range of the applied voltage is 0-10V.

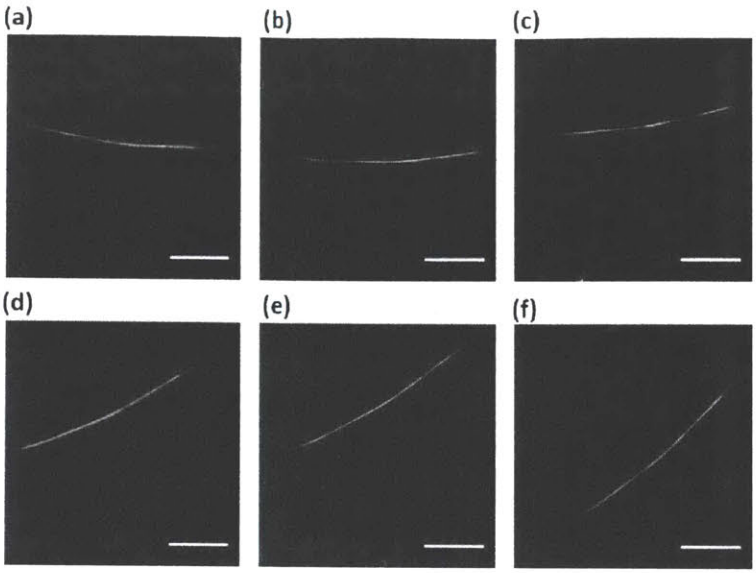

Figure 2-5: the retardance images of an Orange II fiber with different rotation angles. (a)0°; (b)10°; (c)20°; (d) 30°; (e) 40°; (f) 50°. The scale bar is 4 μm. The input power of 633nm laser source is 113 μW. The integration time of the camera is 10ms.

2.4 Experimental Imaging Results

2.4.1 Orange II fibers

Orange II (also called acid orange 7) is a water solvable dye which can be applicable for all kinds of natural wools, cotton and silk ($https://en.wikipedia.org/wiki/Acid_orange_7$) . The commercialized Orange II dye appears to be yellow powders. When mixed into water and heated, Orange II will be resolved by water and turns into orange solution. After the solution cools down, the orange II molecules will assemble to be long polymers. These polymers are finally bundled together and become highly birefringent fibers. We imaged the Orange II fiber with our retardance imaging system producing Figure 2.5. We rotated the fiber over a 50 degrees range and find that the intensity is not changed consistent with the expectation that our measurement is only sensitivity to retardance but not orientation angle of the fiber. The Orange II fibers are illuminated with the super-continuum laser at the wavelength of 633 nm, and the input power is 113 μW. The integration time of the camera is 10ms.

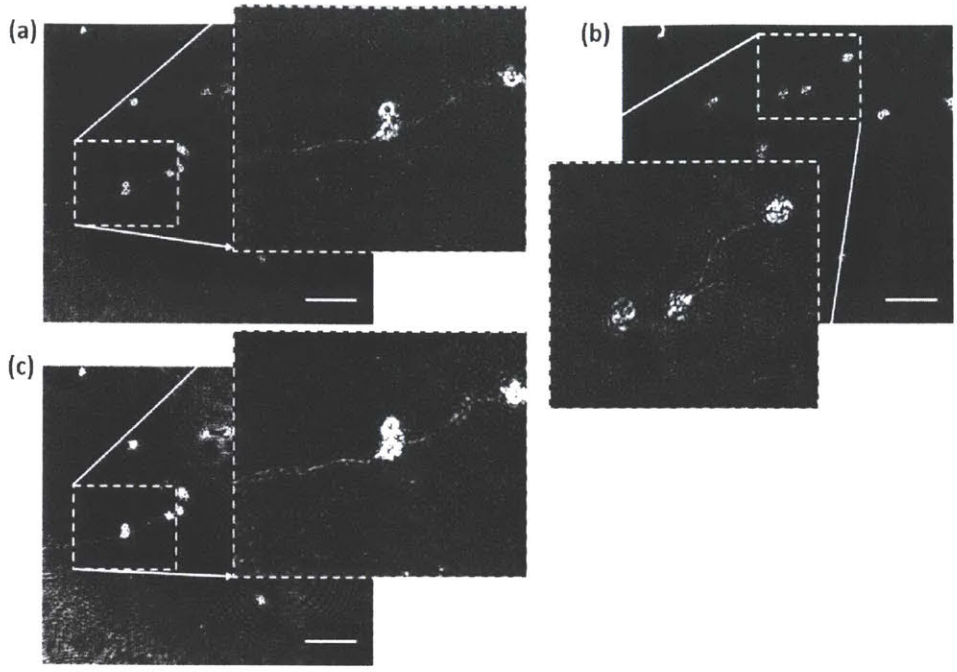

Figure 2-6: the retardance images of crab acrosomes. (a)and(b) the images taken with an integration time of 10ms. The 'tail' part is zoomed in. (c) the image taken with an integration of 100ms. The scale bar is 24μm.

2.4.2 Horse crab sperms

For the sperms of the horseshoe crabs, upon they contact with the egg jelly coat, a bundle of actin filaments cross-linked by scruin-CaM heterodimers extends from the head of the sperm through a nuclear channel to form a 60μm-long finger of membrane[77–79]. This process is called acrosome process. This bundle of actin filaments has a strong birefringent signal since they are highly anisotropic. We demonstrate the retardance imaging results of the horseshoe crab sperms in Figure 2.6. The acrosome has a very strong signal, since the actin bundle is coiled in the head of the sperm. However, we still can detect the birefringent signal from the tail. With longer integration time of the camera, the background of the image will increase, but the signal-to-noise ratio will also be improved.

Chapter 3

Quantitative Polarization Interference Microscopy (QPIM)

3.1 System Design

The experiment setup for QPIM is shown in Figure 3.1, where a fiber-coupled single-mode 633 nm He-Ne laser is used as the illumination source. After the fiber, the laser beam is collimated with a diameter of approximately 5 mm. A circular polarizer is used to convert the collimated laser beam into right-handed circular polarization before illuminating the sample. After transmitting through the sample, the beam is then collected by an objective lens (Olympus, 4X, numerical aperture (NA) = 0.16). A Wollaston prism (WP10P, Thorlabs), placed at the intermediate image plane, decomposes the sample beam into horizontally and vertically polarized beams (oscillating along x and y axes, respectively). These two beams (i.e., the ordinary beam and extraordinary beams) are symmetrically separated along the optical axis with a separation angle of 19.69 degrees at the wavelength of 633nm (the separation angle originates from Thorlabs' specification literature of the Wollaston prisms). A cross-section of the Wollaston prism for illustrating its working principle is shown as an inset figure, where we have defined the x-y-z coordinate system. Next, the two beams pass through a 4f system and impinge on a linear polarizer (LP) before interfering on a CMOS camera (Pointgrey, FL3-U3-13Y3M-C; full frame 1024×1280

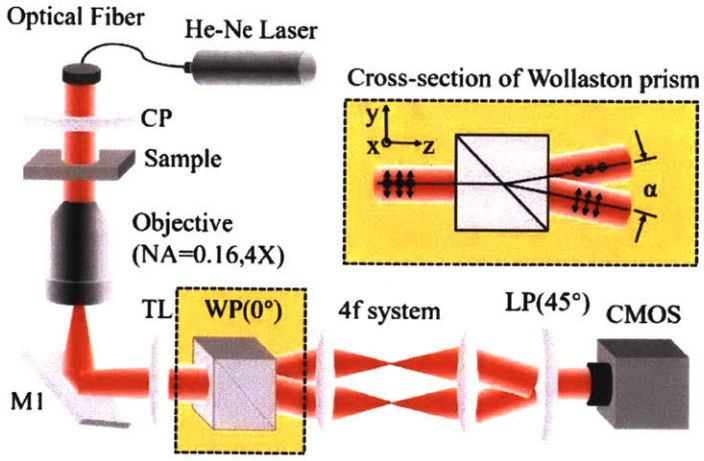

Figure 3-1: Quantitative polarization interference microscope. CP, circular polarizer; TL, tube lens; M1, silver mirror; WP, Wollaston prism; LP, linear polarizer. The transmission axis of the LP is set at 45 degrees in the x-y plane. The inset figure shows the cross-section of the Wollaston prism; the circles indicate the polarization along the x-axis and bidirectional arrows represent the polarization along the y-axis. For the selected Wollaston prism, the divergence angle is 19.69 degrees for 633 nm light. The focal length of the tube lens is 200 mm, and the focal lengths of the two lenses used in 4f system are both 150 mm.

pixels; pixel size 4.8 μm$\times$4.8 μm) at the final image plane, closely after the LP. For intensity matching, the transmission axis of the linear polarizer set at 45 degrees with respect to the x-y plane. The measurement involves recording a fringe patterns (i.e., an interferogram), which is then used to retrieve the complex fields with a Fourier transform method. In order to extract the birefringence parameters, we have developed a new polarization recovery algorithm described in the section as follows.

3.2 The Polarization Recovery Algorithm

After a plane wave transmits through a transparent anisotropic sample, the spatial variation of the birefringence properties will mostly induce a change in the wavefront of the illumination wave. Therefore, compared with light intensity, the complex field reveals more information of the sample, such as sample thickness and birefringence distributions. Conventional polarization microscopes give qualitative sample information as they only measure the modified intensity maps. In order to recover the

polarization parameters (i.e., retardance and orientation angle) in a quantitative fashion, multiple intensity measurements and a complex system are currently deployed. Interferometric microscopy such as QPM allows us to retrieve the complex scattered field from the sample in a single shot. Integrating polarization sensitive optical elements in an interferometric microscope will enable us to retrieve the birefringence information from the complex electric field due to the interference of the ordinary and the extraordinary sample beams. The retardance and the orientation angle distributions are coupled in the real and the imaginary parts (or amplitude and phase) of the transmitted field. In the following, we introduce an algorithm to recover both the retardance and the orientation angle distributions of the sample from the measured interferogram. After a Fourier transform of the interferogram, we obtained the 0^{th} order (i.e. DC term), $+1^{st}$ order and -1^{st} order terms. The $+1^{st}$ (or the -1^{st}) order term gives the complex electric field, $U(x,y)$

$$U(x,y) = B(x,y) + iC(x,y), \tag{3.1}$$

where $B(x,y)$ and $C(x,y)$ are the real and the imaginary parts of the retrieved electric field. After the formulation (see details in Methods Section 1), the retardance distribution of the sample,$\Delta(x,y)$, can be recovered as:

$$\Delta(x,y) = cos^{-1}\left[-\frac{2C(x,y)}{A(x,y)}\right], \tag{3.2}$$

where $A(x,y)$ is the intensity of the 0^{th} order term. Furthermore, the orientation angle distribution, $\varphi(x,y)$ can be calculated as:

$$\varphi(x,y) = \frac{1}{2}cos^{-1}\left[-\frac{2B(x,y)}{\sqrt{A^2(x,y) - 4C^2(x,y)}}\right]. \tag{3.3}$$

Note that if the retardance of the anisotropic sample is larger than 2ÏĂ, it will be necessary to unwrap the recovered retardance to obtain the correct retardance distribution (the detailed algorithm is described in the Methods Section A centered around Equation 3.14). By extracting the real and the imaginary parts of the complex

field, we obtain two equations to decouple the retardance and the orientation angle. The intensity distribution in the 0^{th} order image is used to eliminate the effect of the intensity transmittance through the sample. Equations 3.2 and 3.3 have allowed us to retrieve the retardance and the orientation angle maps with a single image acquisition. The accuracy and efficiency of our algorithm will be explored in the following section.

3.3 Experimental Results

To verify the imaging concept of QPIM, we first measured a calibrated 633 nm zero-order quarter-wave plate (WPQ10ME-633, Thorlabs). We rotated the wave plate's fast axis from 0 to 180 degrees with respect to the x-axis and acquired one interferogram for each 10 degrees increment. Applying our imaging algorithm on this interferogram, we retrieved the retardance and the wave plate orientation angle (i.e., the angle between the x axis and the fast axis of quarter-wave plate). In Figure 3.2a, the recovered average retardance as a function of the sample rotation angle is plotted in red circles, and the actual retardance is plotted in a blue dashed line. From this measurement, the retardance of the quarter-wave plate is determined to be $(0.51\pm0.02)\pi$ radians which is in a good agreement with the actual retardance of 0.5π. The recovered orientation angle (in red circles) and the actual orientation angle (in a blue dashed line) as a function of the rotation angle is presented in Figure 3.2b. Again, we have observed a close match between the measured and the actual values, and the standard deviation of the difference between the recovered and the actual orientation angles is 3.11 degrees ($\sim$ 54 mrad). These results have shown that our system can measure retardance and orientation angle simultaneously with an error around 50-60 mrad. Note that the resolution of the rotation stage (CRM1, Thorlabs) is 2 degrees. To further improve the measurement accuracy, the sample tilt and defocus effect and the resolution and the rotation stage may need to be taken into consideration.

Birefringence properties are widely explored for making precision optical devices such as LC devices and spatial light modulators (SLMs), but there is always a

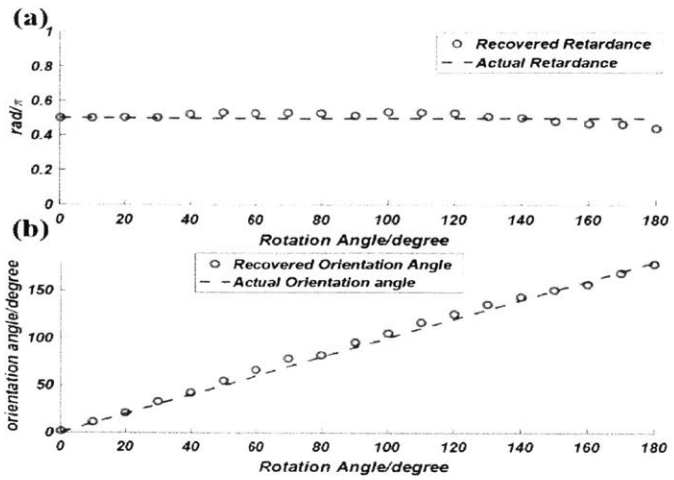

Figure 3-2: The recovered retardance and orientation angle of the fast axis of a quarter-wave plate as a function of the rotation angle from 0 to 180 degrees with 10 degrees increment. (a) Retardance of wave plate measured using QPIM. Each red circle is an average value of the recovered retardance distribution. The blue dashed line represents the actual retardance of the quarter-wave plate which is $\pi/2$. (b) Wave plate's orientation angle recovered using QPIM (red circles). The blue dashed line shows the relation of the actual and the measured rotation angle.

need for better metrology methods to characterize such polarization-sensitive devices. Ellipsometry-based techniques are normally used for inspecting those devices, but they have a low throughput and a small field of view. Polarization-sensitive optical coherence tomography (OCT) systems can be potentially applied to mapping the birefringence distributions, but its point scanning imaging mode will still limit the throughput. On the other hand, our QPIM can achieve full-field and high-speed mapping of the birefringence distributions with a single-shot image capture, which will be specifically validated with our experiments for the characterization of LC samples in the following. First, we illustrate the retardance and the orientation angle parameters in an LC sample with the help of Figure 3.3a. When the light polarization (extraordinary beam) is along the long axis of an LC molecule, the refraction index is n_e while the refraction index is n_o when the light polarization (ordinary beam) is orthogonal to the long axis (i.e., along the short axis). The LC molecule is not necessarily oriented in the observation x-y plane, thus we need to first project the LC molecule orientation into the x-y plane. Then, the angle between the x axis and the

long axis is defined as the orientation angle φ. The phase difference between ordinary and extraordinary beams in the x-y plane is the retardance Δ. In our experiment, we measure the x-y plane distributions of φ and Δ . A custom-made single layer nematic-LC sample (prepared by Hamamatsu Photonics; refer to Methods Section B for LC sample preparation), as shown in Figure 3.3b, is characterized with our system. In this sample, the LC molecules are uniformly distributed between two quartz glass plates and divide into two regions. Each region has a separate pair of electrodes; the device can be considered as an SLM with just two macro pixels. The LC sample thickness is 20 μm whereas the birefringence (difference of n_e and n_o) is 0.2. Therefore, the maximum possible retardance is 39.7 rad. After mounting the sample on our QPIM system and connecting the electrodes, we obtained the interferogram image of the LC boundary region (note that this is the boundary of the two macro pixels) as shown in Figure 3.3c, where a zoom-in image clearly shows the fringes. The right-hand side of the interferogram corresponds to the region, where a zero-centered rectangular voltage wave is applied through a function generator (DS345, Stanford Research Systems). The voltage wave has an amplitude of 3 V and a frequency of 1 kHz. A 2D Fourier transform of the interferogram is performed and the logarithm of its magnitude is shown in Figure 3.3d. By selecting and shifting the 1_{st} order into the center and performing an inverse Fourier transform, we retrieve the complex sample field. The sample retardance is recovered using Equation 3.2, and the result is shown in Figure 3.3e. As the retardance is much larger than 2π, we have developed a method (discussed in the Methods Section 1) combined with the Goldstein algorithm to unwrap the retardance for obtaining the correct measurement result as shown in Figure 3.3f. The average retardance difference between the left and the right regions is 26.4 rad. With no voltage applied to the left region, the retardance of this region remains at the original value of 39.7 rad. The LC molecules in the right region are elevated due to the external electric field, thus resulting in a decrease of the retardance down to 13.3 rad. The orientation angle distribution is retrieved using Equation 3.3, which is shown in Figure 3.3g. From this image, we found the average orientation angle distribution is about 116.3 degrees with a standard deviation of 1.5

degrees. In Figure 3.3h, we show a quiver plot of the retardance and the orientation angle for a $24\mu m \times 18\mu m$ region across the boundary, indicated in the white box in Figure 3.3f. Figure 3.3h shows that the orientation angle is uniformly distributed, and it only deviates around the boundary.

When the applied voltage increases, the LC molecules tilt toward the z-axis, thus resulting in a decrease of sample retardance. If the elevation angle of the LC molecules is 90 degrees, the LC sample will essentially become isotropic with zero retardance. However, in practice, the elevation angle will not become 90 degrees even when maximum allowable voltage is applied. Knowing the elevation angle distributions is important for many applications, such as characterizing linearly photopolymerized liquid crystal polymer films designed to increase the field of view of liquid crystal displays. Next, we measured the LC sample's birefringence response to voltage changes. As we increased the applied voltage of the LC sample right region from 2.3 V to 5 V, we acquired images for every 0.1 V increment. With our imaging algorithm, both the retardance and the orientation angle distributions were retrieved. In Figure 3.4a, we show the recovered retardance map for the initial applied 2.3 V voltage. In the right region an area is selected, as indicated in the white box, for illustrating the birefringence responses to voltage. The spatially averaged retardance and orientation angle values of this selected area are plotted as a function of the applied voltage as shown in Figures 3.4b and c, respectively. In those plots, the blue curves represent the 2nd order polynomial fits. In Figure 3.4b, we observe an expected decrease in retardance, which tends to saturate as a function of time. The standard deviation of the difference of experimental values and the 2^{nd} order polynomial fitting curve is less than 90 mrad. Figure 3.4c shows the observation plane orientation angle at 115.8 ± 3.1 degrees, which is does not change as expected. Typically, the retardance of a LC sample can be characterized by simply measuring the intensity of transmitted light as a function of voltage when the LC is placed between two linear polarizers with a 45 degrees transmission axes mismatch. We performed such an experiment using QPIM and have presented the results in the blue dashed line in Figure 3.4d, where the right vertical axis represents the intensity. While the intensity measurements cannot be

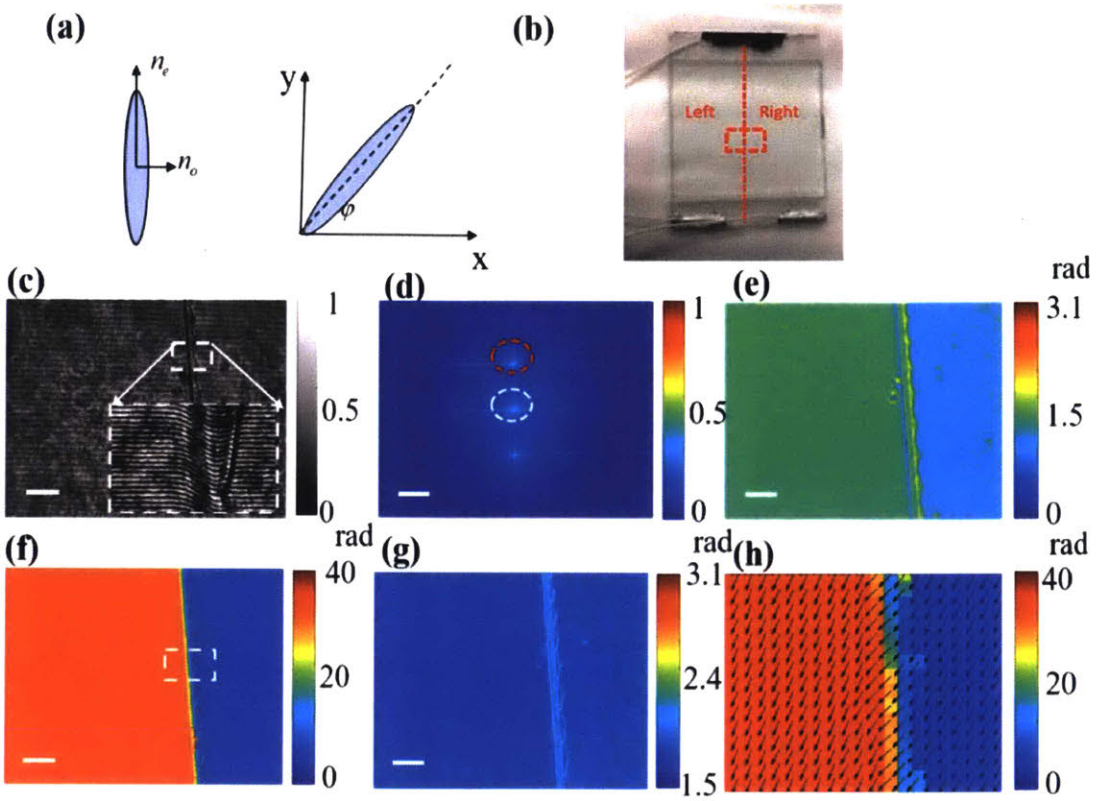

Figure 3-3: LC birefringence characterization using QPIM. (a) An illustration of the retardance and the orientation angle in a LC sample. (b) The customized one-layer nematic-LC sample used in our experiment. The region marked in the red box is imaged with QPIM. (c) Full frame of the LC sample's interferogram. A 3V 1 kHz rectangular voltage wave is applied to the right-hand side of the LC sample, while the left-hand side is connected to the ground. We can clearly observe the boundary of the two macro pixels. Part of the boundary is zoomed in to show the high contrast fringes. (d) The logarithm of the magnitude of the 2D Fourier transform of the interferogram. The white circle marks the 0th order, and the red circle marks the 1^{st} order. Recovered retardance distribution (e) before and (f) after unwrapping. (g) The recovered orientation angle distribution. (h) The quiver plot of the retardance and the orientation angle distributions for a selected $24\mu m \times 18\mu m$ region as indicated in the white box in (f). The color shows the magnitude of the retardance and the arrows show the orientation of the LC molecules. The scale bar in (c) and (e)-(g) is 100 μm, while the scale bar in (d) represents 0.01 μm^{-1}.

used to directly obtain the quantitative retardance curve, our system readily provides quantitative retardance which can be used to obtain the intensity curve in the red dashed line that matches well with the blue curve. This experiment again confirms the quantitative nature of QPIM.

When the applied voltage on the LC sample is suddenly changed, there is a fast-transient change in its birefringence distribution, which can be captured with QPIM due to its high-speed imaging capability. To demonstrate this capability, we recorded interferograms at 150 frames per second (fps) while changing the applied voltage to the right region from 2 V to 3 V with the function generator. The integration time of the camera is approximately 7 ms. The recovered retardance distributions in natural logarithm scale for time points at 1.85 sec, 1.92 sec and 1.95 sec are shown in Figures 3.5a-c, where the imaging area shows the boundary between voltage-controlled and uncontrolled region. Note that we took the natural logarithm of the unwrapped retardance for better observation of the small retardance variances on the right side. The time sequence of the recovered average retardance is shown in Figure 3.5d, from which we noticed that the retardance transition time is between 0.05 and 0.1 sec, which is caused by either the voltage source or the mechanical rotation of LC molecules.

3.4 Conclusions

In this article, we have proposed and demonstrated a novel optical anisotropy imaging technique, QPIM, for fast mapping the birefringence distributions of anisotropic samples. A mathematical model has been developed to retrieve the retardance and the orientation angle distributions from the single-shot interferogram measurements. The single-shot nature of QPIM allows for fast mapping of the retardance and the orientation angle distributions: a feature that has unique potential for many material metrology applications. We have experimentally demonstrated one such metrology application of QPIM, i.e., characterizing LC samples. We envision that QPIM will find promising applications in high-speed imaging of fast dynamics in anisotropic

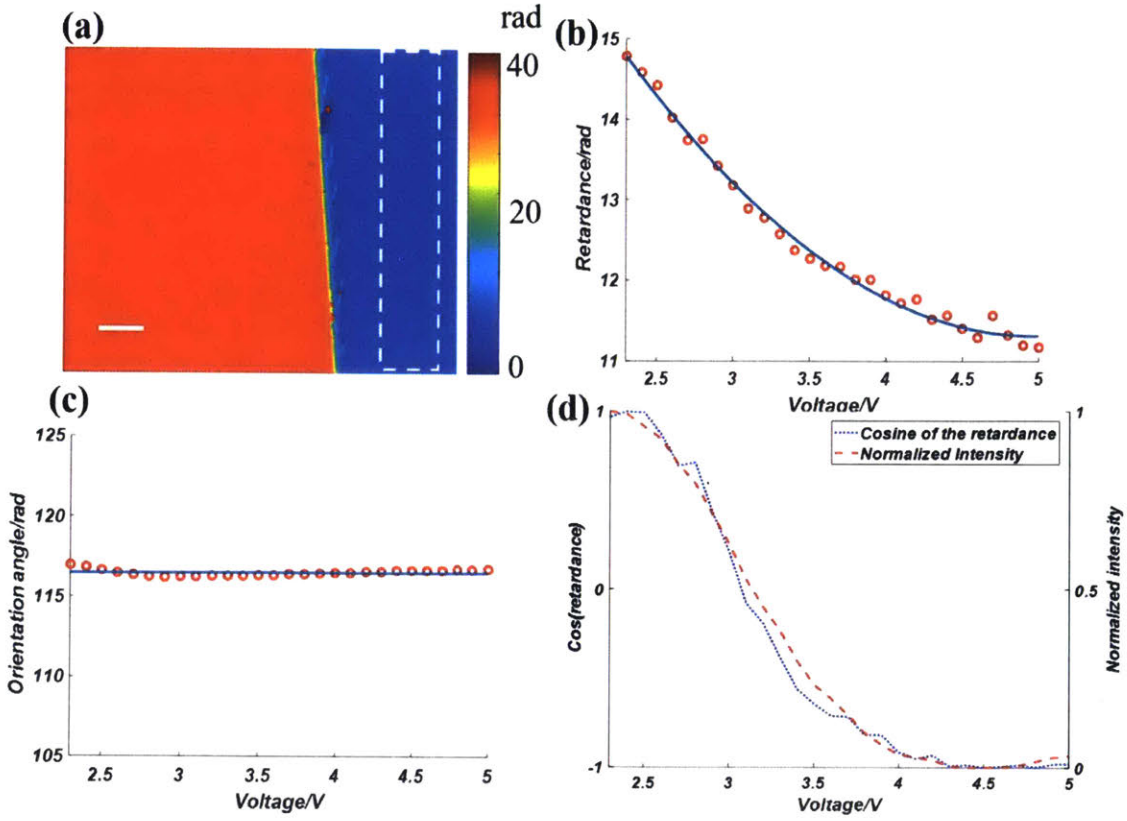

Figure 3-4: Measured voltage response of the retardance and the orientation of custom-built LC sample. (a) The recovered retardance map when the initial 2.3 V voltage is applied to the right region. (b) The voltage response of the recovered average retardance for the region shown in (a). The red dots are the experimentally measured values, and the blue line is the fitted 2^{nd} order polynomial curve. (c) The voltage response of the recovered average orientation angle for the region shown in (a). The red dots are the experimentally measured values, and the blue line is a constant orientation at 115.8 degrees. (d) The blue dashed curve is the measured LC sample intensity transmission versus the applied voltage using two polarizers whose orientation mismatch is 45 degrees. The red dashed curve is the intensity transmission, calculated from measured retardance values, versus the applied voltage.

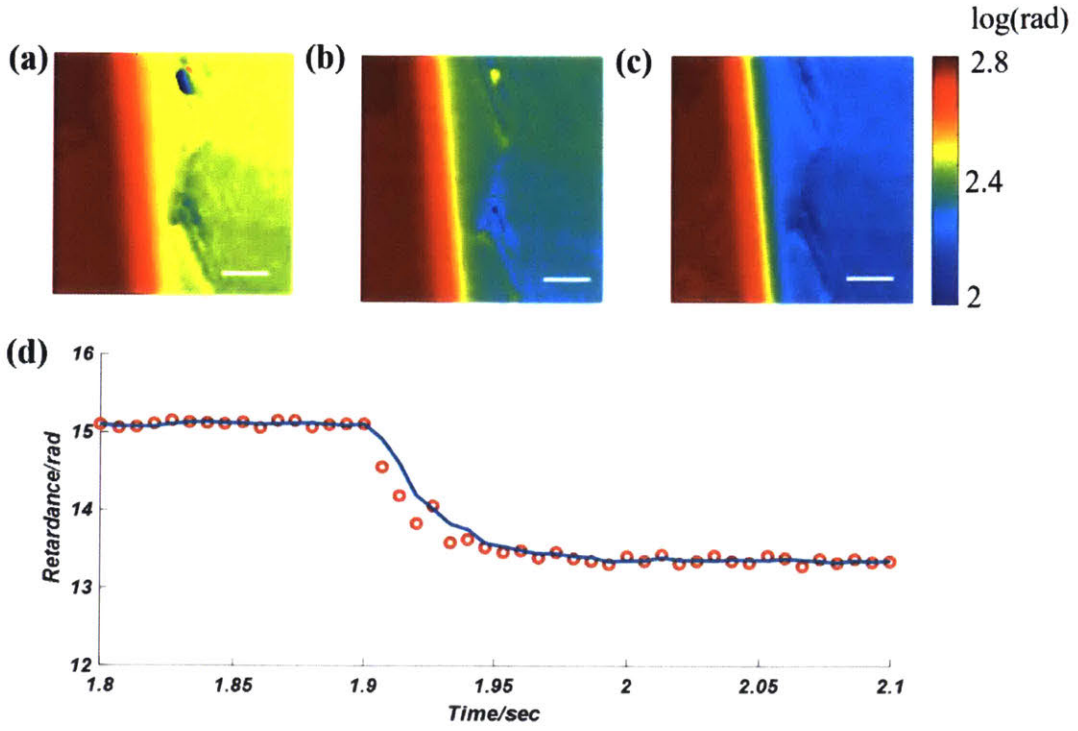

Figure 3-5: The transient dynamics of the retardance distribution due to a sudden voltage change created through the function generator. (a)-(c) The unwrapped retardance distributions (in natural logarithm scale) of a small boundary region for time points at 1.85 sec, 1.92 sec, and 1.95sec, respectively. (d) The time sequence of the recovered average retardance of the right region. The red dots represent the calculated retardance values, while the blue curve is after the average filter. The scale bar denotes 50 μm.

materials and biological samples.

3.5 Methods

3.5.1 Derivation of the interferogram

Jones calculus is applied to trace the complex electric field in the QPIM system. A mathematical algorithm based on digital holography is proposed to extract the birefringence parameters from the measured complex electric field. Firstly, the right-handed circularly polarized illumination light, $\mathbf{E}_{in}$, can be expressed as a Jones vector:

$$\mathbf{E}_{in} = \frac{1}{\sqrt{2}} \begin{pmatrix} 1 \\ -i \end{pmatrix}. \tag{3.4}$$

The axes of Wollaston prism are aligned parallel to the x and y axes as shown in Figure 3.1, and the orientation of the LP is set at 45 degrees to the x axis in the x-y plane. Then, the Jones matrices of the Wollaston prism and the linear polarizer are determined to be:

$$J_{wollaston} = \frac{1}{\sqrt{2}} \begin{pmatrix} e^{jkx} & 0 \\ 0 & 1 \end{pmatrix}, \qquad J_{LP} = \frac{1}{2} \begin{pmatrix} 1 & 1 \\ 1 & 1 \end{pmatrix}, \tag{3.5}$$

where $k = k_0 \sin\alpha$, $k_0 = 2\pi/\lambda$, is the wavelength of the laser in free space, and α is the divergence angle of the Wollaston prism. α and the 4f system following the Wollaston prism determine the period of the interferogram captured on the camera. Next, we derive the Jones matrix of the birefringence sample. The birefringence of the sample contains two parameters: retardance and orientation angle. Taking a single LC molecule orientated in the x-y plane as an example (Figure 3.3a), at each point the retardance, $\Delta(x, y)$, is defined as the difference between the extraordinary light phase delay, $\phi_e(x, y)$, and the ordinary light phase delay, $\phi_o(x, y)$, i.e., $\Delta(x, y) = \phi_e(x, y) - \phi_o(x, y)$. At each point, the orientation angle, $\varphi(x, y)$, is defined as the angle between the long axis of the LC molecule and the x-axis. The retardance and orientation angle at each sample point will be retrieved in QPIM, thus giving a

2D distribution for each parameter. Note that as the size of a single LC molecule is beyond the diffraction limit of the microscope, the measured birefringence parameters are the spatially average values within one diffraction spot. At the end, the Jones matrix of the sample is determined to be:

$$J_{sample} = \begin{pmatrix} \cos\varphi & \sin\varphi \\ -\sin\varphi & \cos\varphi \end{pmatrix} \begin{pmatrix} \exp(i\phi_e) & 0 \\ 0 & \exp(i\phi_o) \end{pmatrix} \begin{pmatrix} \cos\varphi & -\sin\varphi \\ \sin\varphi & \cos\varphi \end{pmatrix}, \quad (3.6)$$

where we neglect (x, y) for simplicity. Finally, the electric field Jones vector at the detector plane is calculated as:

$$\mathbf{E}_{out} = J_{LP} J_{wollaston} J_{sample} \mathbf{E}_{in}, \quad (3.7)$$

where the intermediate Jones matrix J_m of the Wollaston prism and the sample can be written as:

$$J_m = J_{wollaston} J_{sample}$$

$$= \begin{pmatrix} e^{j(\phi_e+kx)}\cos^2\varphi + e^{j(\phi_o+kx)}\sin^2\varphi & -e^{j(\phi_e+kx)}\sin\varphi\cos\varphi + e^{j(\phi_o+kx)}\sin\varphi\cos\varphi \\ -e^{j\phi_e}\sin\varphi\cos\varphi + e^{j\phi_o}\sin\varphi\cos\varphi & e^{j\phi_e}\sin^2\varphi + e^{j\phi_o}\cos^2\varphi \end{pmatrix}. \quad (3.8)$$

Assuming the intensity transmission coefficient at each point on the sample to be $\tau(x, y)$. With the illumination intensity distribution of $I_{in}(x, y)$, which will be assumed uniform, the intensity recorded on the CCD is supposed to be:

$$I(x, y) = \tau(x, y) I_{in}(x, y) \mathbf{E}_{out} \mathbf{E}^*_{out}$$

$$= \tau(x, y) I_{in}(x, y) \left[2 - \cos kx \cos 2\varphi(x, y) \sin\Delta(x, y) \; - \sin kx \cos\Delta(x, y)\right]. \quad (3.9)$$

Note that there is also a background intensity distribution that can be eliminated by subtracting a calibration image. Through recording $I(x, y)$, namely the interferogram image, we can retrieve the complex field $U(x, y)$ from the 1st order signal (detailed in Supplementary Material Section 1), thus giving:

$$U(x, y) = \tau(x, y) I_{in}(x, y)(\cos 2\varphi(x, y) \sin \Delta(x, y) - i \cos \Delta(x, y)). \tag{3.10}$$

We can also recover the original 0^{th} order signal, i.e., the DC term, as:

$$A(x, y) = 2\tau(x, y) I_{in}(x, y). \tag{3.11}$$

The real part of the complex field is

$$B(x, y) = \tau(x, y) I_{in}(x, y) \cos 2\varphi(x, y) \sin \Delta(x, y). \tag{3.12}$$

The imaginary part of the complex field is

$$C(x, y) = -\tau(x, y) I_{in}(x, y) \cos \Delta(x, y) \tag{3.13}$$

With Equations 3.11-13, Equations 3.2-3 can be derived and the retardance and orientation angle distributions can be obtained.

For samples like the LC device, the retardance is often quite large (over 2π), but the retardance recovered from Equation 3.2 ranges from $0 - \pi$ due to the property of the function $\cos^{-1}$. The unwrap algorithm we often used is designed to process the wrapped phase, which is retrieved from $\tan^{-1}$, ranging from $-\pi/2$ to $\pi/2$. To unwrap the retardance, we should do the following operation to make the retrieved retardance compatible with unwrap algorithms:

$$\Delta_2(x, y) = \tan^{-1}\left(-\frac{B(x, y)}{C(x, y) \cos 2\varphi(x, y)}\right), \tag{3.14}$$

where $\cos 2\varphi(x, y)$ is calculated with Equation 3.3. It is easier to unwrap $\Delta_2(x, y)$,

since it ranges from $-\pi/2$ to $\pi/2$ so that we can directly use Goldstein's algorithm.

3.5.2 Sample Preparation

The LC sample used to verify our method is specially designed at Hamamatsu Photonics. A LC cell was created by bonding two quartz glass plates together with 20 Âţm cell gap between. Both sides of the glass plates were coated with a wide-range anti-reflective coating, a high-resistance Indium Tin Oxide (ITO) conductive layer, and a Polyimide (PI) alignment layer on internal surface of the cell. In the following, we list the steps for filling the cell with LC:

1. PI layer were rubbed and assembled for parallel alignment of the LC.
2. Arbitrary electrodes were fabricated on the ITO layer with femtosecond laser processing.
3. Inserted a cell with single filling hole into a vacuum chamber, placed a LC material in a container under the cell.
4. Evacuated the vacuum chamber and heated the container to a temperature above the LC clearing point.
5. After the chamber reached the required vacuum level and temperature, contacted the LC to the filling hole of the cell.
6. Released the pressure in the chamber to fill the cell with LC.

3.6 Sensitivity Analysis

Like other quantitative phase microscope designs, the measurement sensitivity of QPIM can be affected by many environmental factors, such as mechanical vibrations or air density fluctuations. However, when these environmental influences are minimized, the effect of shot noise becomes dominant. According to Poisson statistics, the minimum temporal standard deviation of the intensity can be expressed as:

$$\delta I = \frac{1}{\sqrt{N}}, \tag{3.15}$$

where $N$is the well depth of the camera. For interferograms of near-common-path setups, the intensity distributions can be expressed by (note that for simplicity we consider a one-dimensional signal, but it can be easily extended to 2D signals):

$$I(x) = I_0 \left\{ 1 + \gamma(x) \cos \left[\frac{2\pi}{\Lambda} x + \bar{\phi}(x) \right] \right\}. \tag{3.16}$$

where $I(x)$denotes the interferogram distribution, $I_0$is the average value of the intensity(assume the illumination I_{in} is uniform and the sampleâĂŹs absorption τ is negligible), $\gamma(x)$ and $\bar{\phi}(x)$represent the amplitude and phase of the detected complex field, and is the spatial period of the interferogram. $\bar{\phi}(x)$ is actually the differential phase of two sample beams. Based on our algorithm, we can retrieve the 0^{th} order intensity (i.e., DC term), the real part, and the imaginary part of complex field which can be shown as:

$$\begin{aligned} A(x) &= I_0, \\ B(x) &= \frac{1}{2}\gamma(x) I_0 \cos \phi_s(x), \\ C(x) &= \frac{1}{2}\gamma(x) I_0 \sin \phi_s(x). \end{aligned} \tag{3.17}$$

In Figure 3.6a, we described a simple situation that four camera pixels sample each period of the fringes. We also assume that $I_0 = \frac{1}{2}, \gamma(x) = 1, \phi_s(x) = 0$. The intensities of each pixel are $I_1 = 1$, $I_3 = 0$, $I_2 = I_4 = 1/2$. Therefore, based on previous analysis, A, B, and C can be retrieved as:

$$\begin{aligned} A &= \frac{1}{4}(I_1 + I_2 + I_3 + I_4) = \frac{1}{2}, \\ B &= \frac{1}{2}\frac{I_1 - I_3}{2} = \frac{1}{4}, \\ C &= \frac{1}{2}\frac{I_2 - I_4}{2} = 0. \end{aligned} \tag{3.18}$$

Since the intensity of each pixel is proportional to the number of photons received, following the Poisson statistics the measurement uncertainties of A , B , and C are

$$\delta^2 A = \frac{1}{4}(\delta^2 I_1 + \delta^2 I_2 + \delta^2 I_3 + \delta^2 I_4) \geq \delta^2 I = \frac{1}{N}, \tag{3.19}$$

$$\begin{aligned} \delta^2 B &= \frac{1}{4}\delta^2(I_1 - I_3) = \frac{1}{4}\frac{\delta^2(n_1 - n_3)}{(n_1 - n_3)^2} \\ &= \frac{1}{4}\frac{1}{n_1 - n_3} \geq \frac{1}{4N}, \end{aligned} \tag{3.20}$$

$$\begin{aligned} \delta^2 C &= \frac{1}{4}\delta^2(I_2 - I_4) = \frac{1}{4}\frac{\delta^2(n_2 - n_4)}{(n_2 - n_4)^2} \\ &= \frac{1}{4}\frac{1}{n_2 - n_4} \geq \frac{1}{4N}, \end{aligned} \tag{3.21}$$

We can see that the optimal variances of both $B$and Cequal 1/4N. The DC term of the interferogram, A is the spatial average of the interferogram. We can also assume its uncertainty is the same as the interferogram as shown in Equation 3.22. Therefore, we can conclude that the optimal standard deviations are:

$$\delta A = \delta I = \frac{1}{\sqrt{N}}, \delta B = \delta C = \frac{\delta I}{2} = \frac{1}{2\sqrt{N}}. \tag{3.22}$$

According to the result shown in Equation 3.23 and the principles of error propagation, the uncertainties of recovered retardance and orientation angle are shown below:

$$\delta^2 \Delta = \frac{1}{2A^2}\left(\frac{A + 8C^2}{A - 4C^2}\right)\delta^2 I, \tag{3.23}$$

$$\delta^2 \varphi = \left(\frac{(A^2 + 8B^2)(A^2 - 4C^2)^2 + 16B^2C^2(A^2 + 8C^2)}{2A^2(A^2 - 4B^2 - 4C^2)(A^2 - 4C^2)^2}\right)\delta^2 I. \tag{3.24}$$

Based on Equations 3.11-13, if we assume the transmittance τ of the sample and the illumination intensity distribution I_{in} is uniform, we can rewrite the DC term , real part B, and imaginary part C from the given values of retardance Δ

and orientation angle φ. Therefore, the standard deviations of varying retardance and orientation angle can be simulated, which are shown in Figures 3.6b-d, where we assume the well depth of the camera is 10651 electrons. For the measurement of retardance, the uncertainty is only related to its own actual values. As shown in Figure 3.6b, the retardance measurement is the most accurate when the actual retardance is $\pi/2$ with a standard deviation of 0.014 rad. However, the uncertainty becomes singular when the actual retardance is 0 or π, which means the measurement is not reliable when the anisotropic signal is very weak. For the measurement of orientation angle the situation is more complicated. Its uncertainty relies on both retardance and orientation angle values. The standard deviation of orientation angle becomes singular when the retardance is 0 or π, which is shown in Figure 3.6c. It is reasonable because when the retardance is zero, the measured orientation angle value has no physical meaning (i.e., the sample is essentially isotropic). The standard deviation of orientation is also related to the orientation angle itself, which is shown in Figure 3.6d where the retardance is fixed at $\pi/2$. The uncertainty is singular when the orientation angle is 0 or 90 degrees, which means the measurement of orientation is not reliable when it is parallel to x or y axis defined by the Wollaston orientation. The optimal sensitivity orientation angle is 0.79 degree (0.014 rad) when the retardance is $\pi/2$, and the orientation angle is 45 or 135 degrees. However, these simulated results assume that the depth well is depleted in every pixel of the camera, which is impossible in actual measurements. Therefore, the measured temporal noise is always larger than the calculated one. But we can still learn the trend of the shot noise variation on the dependency of the measured retardance and orientation angles with the simulation results.

To experimentally analyze the temporal uncertainty of the QPIM system, we measured 900 consecutive interferograms on the LCD sample at 150 fps imaging speed while no voltage is applied (this ensures that the retardance is uniform over the whole field of view). After acquiring the interferograms, we retrieved the 0th order intensity (A), and the real part (B) and the imaginary part (C) of the 1st order complex field, and then recover the retardance and the orientation angle distributions

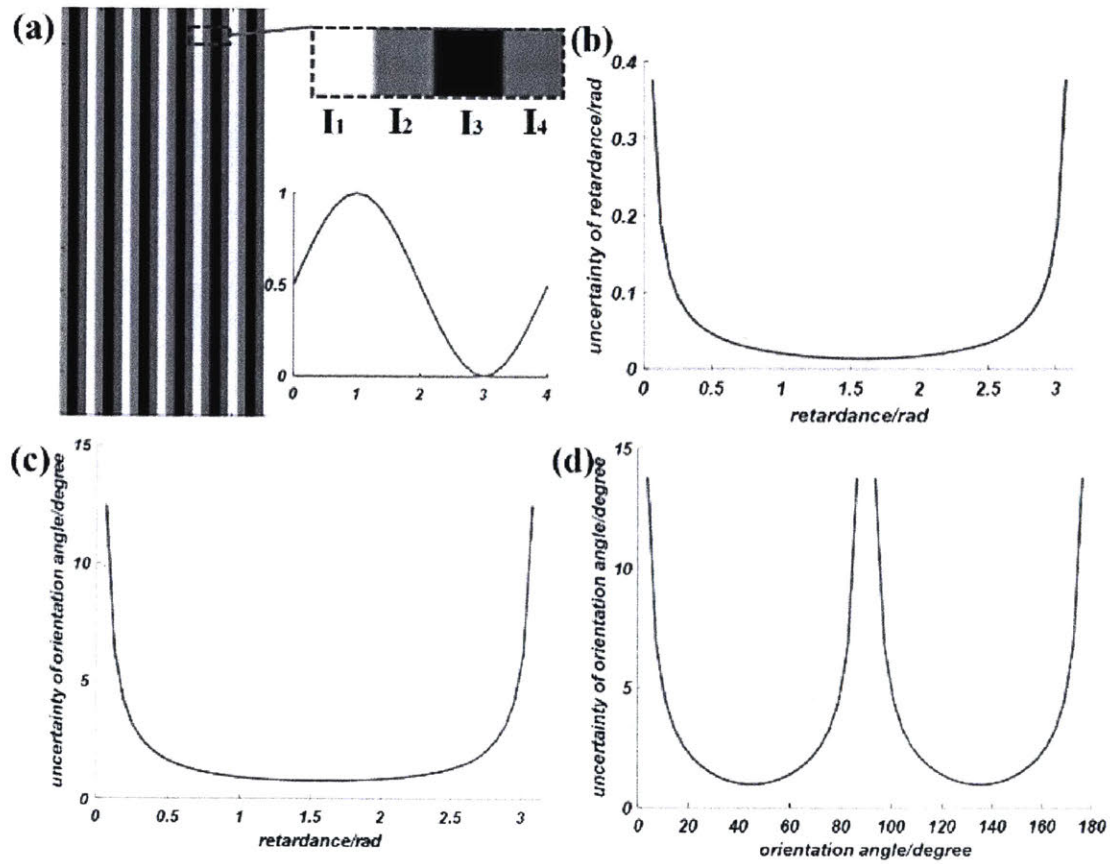

Figure 3-6: Theoretical analysis of QPIM sensitivity. (a) The sketch of the interferogram intensity distribution relative to the well depth of the camera; (b) the relation of the recovered retardance's standard deviation and the actual value of it; (c) the relation of the recovered orientation angle's standard deviation and the actual value of retardance; (d) the relation of the recovered orientation angle's standard deviation and its own actual values.

based on our algorithms (refer to Method Section 1). We pick the sample pixel of each image, record their variations over time. In this way, we can obtain the time lapse and analyze their temporal uncertainties. As shown in Figure 3.7a, the standard deviation of the 0^{th} order intensity (A), and the real part (B) and the imaginary part (C) of the retrieved complex field is 0.011, 0.005 and 0.005, respectively. The well depth for the camera is 10651 electrons, which means that the intensity standard deviation due to the photon shot-noise is 0.0097. The experimentally measured values are slightly larger than expected values of 0.0097 (for A), 0.0049 (for B), and 0.0049 (for C). The reason may be that the electron well is not fully filled. In Figure 3.7b, the temporal uncertainties of the recovered retardance and orientation angle are also experimentally measured, which are 0.04 rad and 2.05 degrees respectively. Also, the histograms of retrieved retardance and orientation angle time series are shown in Figures 3.7c and d. The measured value of retardance and orientation angle are 0.3π rad and 30.6 degrees. From the theoretical frame mentioned in Equations 3.23-24, the corresponding uncertainties for retardance and orientation angle are 0.02 rad and 1.3 degrees. The discrepancies may also due to the insufficiency filling the electron well factors and other systematic errors rooted in the current QPIM system. Nevertheless, we should be mindful that the birefringence uncertainties are dominated by the photon shot noise, which can be only improved by using higher well depth cameras.

To determine the spatial noise of birefringence measurements using our system, we calculated the standard deviation of the a fixed 200 $\times$ 200-pixel region in the recovered retardance, orientation angle, and unwrapped retardance maps. The distributions are measured from the nematic liquid crystal sample, and a uniform region as indicated by white boxes in Fig. S3 is used for calculating the spatial uncertainty values. Figure 3.8a, c, and e show the recovered retardance, orientation angle, and the unwrapped retardance distributions, respectively. Histograms corresponding to the white box regions are generated as shown in Figure 3.8b, d, and f. From the histograms, we determined that the standard deviation of retardance, orientation angle, and unwrapped retardance are 0.0061 rad, 0.40 degrees, and 0.0031 rad. Those values, if translated into optical path differences, are within 0.3-0.6 nm.

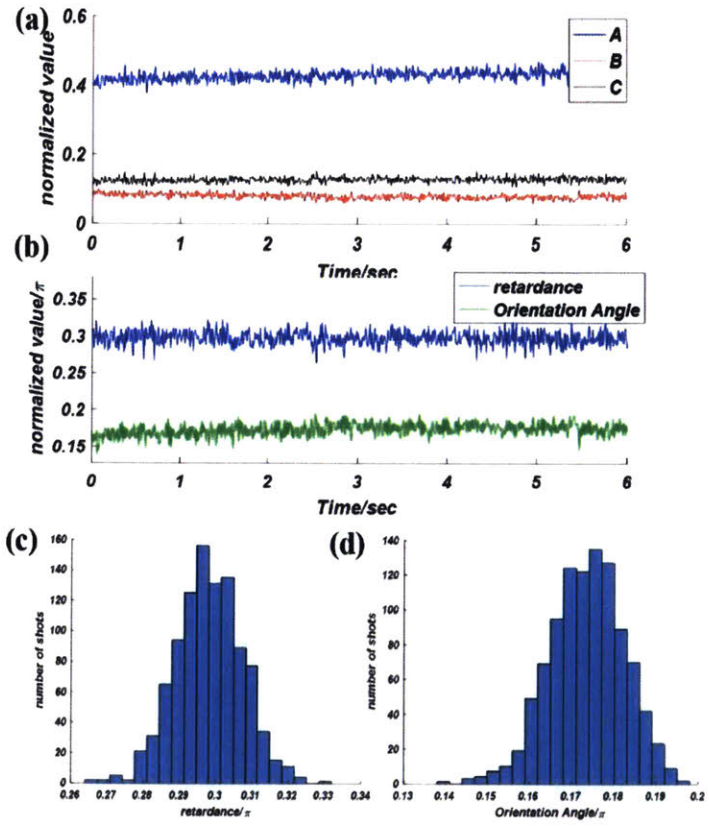

Figure 3-7: Time lapse of birefringence parameters and temporal noise analysis. (a) The time lapse plots of the recovered 0th order intensity(A), and the real part (B) and imaginary part(C) of $+1^{st}$ complex field. (b) The time lapse plots of the retardance and orientation angle. The recording period is 6 seconds at 150 fps (c) the histograms of the retardance and (d) orientation angle time series. The unit of retardance and orientation angle is radiance and divided by π.

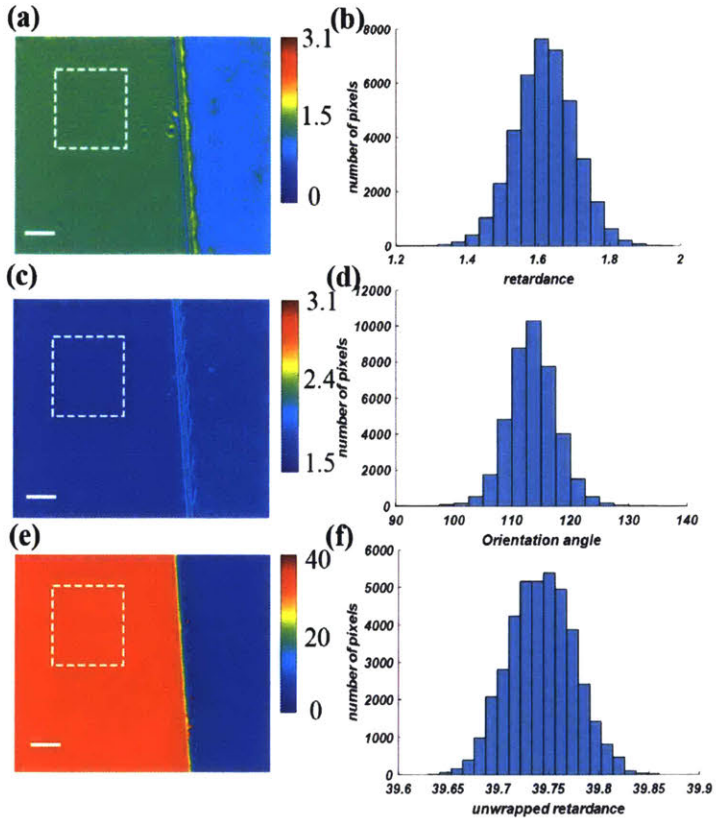

Figure 3-8: Spatial uncertainty analysis of the measured birefringence parameter on a uniform LC region. (a) The recovered retardance distribution; (b) the histogram of the region marked with dashed white line in (a); (c) the recovered orientation angle distribution; (d) the histogram of the white dashed line marked region in (c); (e) the unwrapped retardance distribution; (f) the histogram of the white dashed line marked region in (e).

Chapter 4

Anisotropic Optical Diffraction Tomography

Optical Diffraction Tomography (ODT) has been developed as an efficient method to reconstruct the three-dimensional retraction index distribution of living biological structures[54, 55]. Recently, this method has been widely used for the biological researches, as I mentioned in the introduction part[57]. However, one limitation of this method is that the reconstruction theory of ODT is based an assumption that the refraction index distribution inside the biological samples are isotropic. This assumption is not valid for biological samples such as collagens, cytoskeletons and actins which contain highly anisotropic structures. To image these anisotropic biological samples and retrieve their polarization parameters, a vector-space based diffraction theory is required. Therefore, in this chapter, I demonstrate a three-dimensional polarization parameter (birefringence and orientation angle) reconstruction algorithm developed based on anisotropic Helmholtz equation. The simulation and experimental results have been shown to prove our theory.

4.1 Anisotropic Helmholtz Equation

The nature of light is electromagnetic wave. When light illuminated on biological samples, it will be scattered and interact with the structures inside the cell. This

process can be described concisely with the constitutive relation of the electric field:

$$\mathbf{D} = \varepsilon\mathbf{E} = \varepsilon_0(1+\chi)\mathbf{E}, \tag{4.1}$$

where Eis the electric field, andDis the electric displacement field. εdenotes the dielectric constant, and $\varepsilon_0$is the dielectric constant in the air. χrepresents the electric susceptibility, which is also the scattering potential, directly related to the light scattering in the medium. In anisotropic medium, $\varepsilon$and $\chi$are both tensors. From Maxwell equations, we can derive a wave equation:

$$\nabla^2\mathbf{E}(\mathbf{r},t) = \mu\varepsilon(\mathbf{r})\frac{\partial^2\mathbf{E}(\mathbf{r},t)}{\partial t^2}, \tag{4.2}$$

where μ is the magnetic permeability, which is assumed to be uniform and homogeneous,

$$\mu = \begin{pmatrix} \mu_0 & & \\ & \mu_0 & \\ & & \mu_0 \end{pmatrix}. \tag{4.3}$$

However, the electric permittivity ε is heterogeneous and anisotropic, which can be expressed by the following formula under Cartesian coordinates:

$$\bar{\bar{\varepsilon}}(\mathbf{r}) = \begin{pmatrix} \varepsilon_{xx} & \varepsilon_{xy} & \varepsilon_{xz} \\ \varepsilon_{yx} & \varepsilon_{yy} & \varepsilon_{yz} \\ \varepsilon_{zx} & \varepsilon_{zy} & \varepsilon_{zz} \end{pmatrix}(\mathbf{r}). \tag{4.4}$$

The electric field is also anisotropic and heterogeneous:

$$\mathbf{E}(\mathbf{r},t) = \begin{pmatrix} E_x \\ E_y \\ E_z \end{pmatrix}(\mathbf{r},t). \tag{4.5}$$

Therefore, we can expand the wave equation to be:

$$\begin{pmatrix} \frac{\partial^2 E_x}{\partial x^2} + \frac{\partial^2 E_x}{\partial y^2} + \frac{\partial^2 E_x}{\partial z^2} \\ \frac{\partial^2 E_y}{\partial x^2} + \frac{\partial^2 E_y}{\partial y^2} + \frac{\partial^2 E_y}{\partial z^2} \\ \frac{\partial^2 E_z}{\partial x^2} + \frac{\partial^2 E_z}{\partial y^2} + \frac{\partial^2 E_z}{\partial z^2} \end{pmatrix} = \frac{\partial^2}{\partial t^2} \begin{pmatrix} \mu_0 \varepsilon_{xx} E_x + \mu_0 \varepsilon_{xy} E_y + \mu_0 \varepsilon_{xz} E_z \\ \mu_0 \varepsilon_{yx} E_x + \mu_0 \varepsilon_{yy} E_y + \mu_0 \varepsilon_{yz} E_z \\ \mu_0 \varepsilon_{zx} E_x + \mu_0 \varepsilon_{zy} E_y + \mu_0 \varepsilon_{zz} E_z \end{pmatrix}. \tag{4.6}$$

Then we can assume the electric field is monochromatic, which means:

$$\mathbf{E}(\mathbf{r}, t) = \mathbf{E}(\mathbf{r}) \exp(i\omega t), \tag{4.7}$$

where $\omega$is the angular frequency of the light. Therefore, the monochromatic wave equation becomes Helmholtz Equation:

$$(\nabla^2 + \omega^2 \mu \bar{\bar{\varepsilon}}) \mathbf{E}(\mathbf{r}) = 0. \tag{4.8}$$

4.2 Inverse Scattering Problem

For the consistence of the illustration, we use the vectorial field $\mathbf{U}(\mathbf{r})$to substitute the electric field $\mathbf{E}(\mathbf{r})$. The field measured in the image plane can be assumed as the superposition of the illumination field and the scattered field, which can be expressed by $\mathbf{U}(\mathbf{r}) = \mathbf{U}_i(\mathbf{r}) + \mathbf{U}_s(\mathbf{r})$. $\mathbf{U}_i(\mathbf{r})$is the illumination field and $\mathbf{U}_s(\mathbf{r})$is the scattered field. Recovering the refraction index(or electric permittivity) distribution from the data of measured field is actually an inverse problem. Currently, we only consider about two-dimensional case and the normal incident illumination field. First of all, for the illumination field, the vectorial Helmholtz equation can be written as:

$$\left(\nabla^2 + \omega^2 \mu_0 \varepsilon_0\right) \mathbf{U}_i(\mathbf{r}) = 0, \tag{4.9}$$

In the heterogeneous medium, for the total field, the Helmholtz equation is:

$$\left(\nabla^2 + \omega^2 \mu_0 \bar{\bar{\varepsilon}}(\mathbf{r})\right) \mathbf{U}(\mathbf{r}) = 0, \tag{4.10}$$

Use Eq.(10) to subtract Eq.(9), and we assume that $|\mathbf{U}_i(\mathbf{r})| \gg |\mathbf{U}_s(\mathbf{r})|$ based on Born approximation. Therefore, we can derive the following equation[74]:

$$\nabla^2 \mathbf{U}_s(\mathbf{r}) + \omega^2 \mu_0 \varepsilon_0 \mathbf{U}_s(\mathbf{r}) = -\omega^2 \mu_0 \left(\overline{\overline{\varepsilon}}(\mathbf{r}) - \varepsilon_0\right) \mathbf{U}_i(\mathbf{r}), \tag{4.11}$$

From Eq. (1), and we know that $\omega^2 \mu_0 \varepsilon_0 = \omega^2/c^2 = \left({}^{2\pi}/_{\lambda}\right)^2 = \beta^2$, where $\beta$is the wave number, we can rewrite Eq. (4.11) to be:

$$\nabla^2 \mathbf{U}_s(\mathbf{r}) + \beta^2 \mathbf{U}_s(\mathbf{r}) = -\beta^2 \overline{\overline{\chi}}(\mathbf{r}) \mathbf{U}_i(\mathbf{r}), \tag{4.12}$$

where $\overline{\overline{\chi}}(\mathbf{r})$is the electric susceptibility, also the scattering potential. $\overline{\overline{\chi}}(\mathbf{r})$is also a tensor in the anisotropic medium. The scalar solution for Eq. (4.12) in frequency domain is shown below, which is derived under the theory of optical diffraction tomography:

$$\tilde{\chi}(k_x, k_y, q - \beta) = \frac{i\pi q}{\beta^2} \tilde{U}_s(k_x, k_y; z = 0). \tag{4.13}$$

The diffraction effect is also considered in this algorithm. However, when the numerical aperture of the microscope objective is small, we can approximately believe that the retrieved scattering potential distribution is at $z = 0$ plane.

4.3 Retardance and Orientation Angle Retrieval Algorithm

We can expand Eq. (4.12) in a 2D circumstance:

$$\nabla^2 \begin{pmatrix} U_{sx}(\mathbf{r}) \\ U_{sy}(\mathbf{r}) \end{pmatrix} + \beta^2 n_m^2 \begin{pmatrix} U_{sx}(\mathbf{r}) \\ U_{sy}(\mathbf{r}) \end{pmatrix} = -\beta^2 \begin{pmatrix} \chi_{xx}(\mathbf{r}) & \chi_{xy}(\mathbf{r}) \\ \chi_{yx}(\mathbf{r}) & \chi_{yy}(\mathbf{r}) \end{pmatrix} \begin{pmatrix} U_{ix} \\ U_{iy} \end{pmatrix}, \tag{4.14}$$

If the illumination field is $\mathbf{U}_i(\mathbf{r}) = \frac{1}{\sqrt{2}}(1,1)^T \exp(i\beta z)$, we can have:

$$(\nabla^2 + \beta^2 n_m^2) U_{sx1}(\mathbf{r}) = -\frac{\beta^2}{\sqrt{2}} (\chi_{xx}(\mathbf{r}) + \chi_{xy}(\mathbf{r})) \exp(i\beta z),$$

$$(\nabla^2 + \beta^2 n_m^2) U_{sy1}(\mathbf{r}) = -\frac{\beta^2}{\sqrt{2}} (\chi_{yx}(\mathbf{r}) + \chi_{yy}(\mathbf{r})) \exp(i\beta z). \tag{4.15}$$

According to the theory of optical diffraction tomography, we can solve the scattering potential in frequency domain:

$$(\tilde{\chi}_{xx} + \tilde{\chi}_{xy})(k_x, k_y, q - \beta) = \frac{i\sqrt{2}\pi q}{\beta^2} \tilde{U}_{sx1}(k_x, k_y; z = 0)$$

$$(\tilde{\chi}_{yx} + \tilde{\chi}_{yy})(k_x, k_y, q - \beta) = \frac{i\sqrt{2}\pi q}{\beta^2} \tilde{U}_{sy1}(k_x, k_y; z = 0) \tag{4.16}$$

where $q = \sqrt{\beta^2 n_m^2 - k_x^2 - k_y^2}$. Similarly, if we use $\mathbf{U}_i(\mathbf{r}) = \frac{1}{\sqrt{2}}(1, -1)^T \exp(i\beta z)$, we can solve the left two components in the scattering potential matrix with:

$$(\tilde{\chi}_{xx} - \tilde{\chi}_{xy})(k_x, k_y, q - \beta) = \frac{i\sqrt{2}\pi q}{\beta^2} \tilde{U}_{sx2}(k_x, k_y; z = 0)$$

$$(\tilde{\chi}_{yx} - \tilde{\chi}_{yy})(k_x, k_y, q - \beta) = \frac{i\sqrt{2}\pi q}{\beta^2} \tilde{U}_{sy2}(k_x, k_y; z = 0) \tag{4.17}$$

Therefore, the total expression of retrieving the scattering potential matrix is:

$$\begin{pmatrix} \tilde{\chi}_{xx} & \tilde{\chi}_{xy} \\ \tilde{\chi}_{yx} & \tilde{\chi}_{yy} \end{pmatrix} (k_x, k_y, q - \beta) = \frac{i\pi q}{\sqrt{2}\beta^2} \begin{pmatrix} \tilde{U}_{sx1} + \tilde{U}_{sx2} & \tilde{U}_{sx1} - \tilde{U}_{sx2} \\ \tilde{U}_{sy1} + \tilde{U}_{sy2} & \tilde{U}_{sy1} - \tilde{U}_{sy2} \end{pmatrix} (k_x, k_y; z = 0). \tag{4.18}$$

If we know the full matrix of scattering potential, the eigenvalue(χ_e and χ_o) and the rotation matrix can be retrieved by diagonalization. This process can be shown by:

$$\begin{pmatrix} \chi_e(\mathbf{r}) & 0 \\ 0 & \chi_o(\mathbf{r}) \end{pmatrix} = \begin{pmatrix} \cos\varphi(\mathbf{r}) & -\sin\varphi(\mathbf{r}) \\ \sin\varphi(\mathbf{r}) & \cos\varphi(\mathbf{r}) \end{pmatrix} \begin{pmatrix} \chi_{xx}(\mathbf{r}) & \chi_{xy}(\mathbf{r}) \\ \chi_{yx}(\mathbf{r}) & \chi_{yy}(\mathbf{r}) \end{pmatrix} \begin{pmatrix} \cos\varphi(\mathbf{r}) & \sin\varphi(\mathbf{r}) \\ -\sin\varphi(\mathbf{r}) & \cos\varphi(\mathbf{r}) \end{pmatrix}. \tag{4.19}$$

It worth notice that $\chi_{xy}(\mathbf{r}) = \chi_{yx}(\mathbf{r})$, since the scattering potential matrix is symmetric. Therefore, the retardance(RI difference) and orientation angle can be retrieved with:

$$\Delta n(\mathbf{r}) = n_e(\mathbf{r}) - n_o(\mathbf{r}) \approx \frac{\left(\chi_{xx}(\mathbf{r}) - \chi_{yy}(\mathbf{r})\right)^2 - 4\chi_{xy}^2(\mathbf{r})}{2n_m\sqrt{\left(\chi_{xx}(\mathbf{r}) - \chi_{yy}(\mathbf{r})\right)^2 + 4\chi_{xy}^2(\mathbf{r})}},$$

$$\varphi(\mathbf{r}) = \frac{1}{2}\arctan\left(\frac{2\chi_{xy}(\mathbf{r})}{\chi_{yy}(\mathbf{r}) - \chi_{xx}(\mathbf{r})}\right). \tag{4.20}$$

4.4 Three-dimensional Reconstruction with Angle-scanning tomography

To retrieve the three-dimensional distribution of birefringence and orientation, we should consider about the theory of angle-scanning optical diffraction tomography[54, 55]. Generally speaking, the coherent transfer function of an optical system is the head of a sphere in frequency domain. The radius of this sphere is determined by the illumination wavelength and the range of the head is related to the numerical aperture. If the illumination angle is changed, the position of the sphere is shifted and we can detect different spatial frequency of the sample three-dimensionally.

If the wave vector of the illumination field becomes $\mathbf{k}_i = \begin{pmatrix} k_{ix} & k_{iy} & k_{iz} \end{pmatrix}^T$, where $k_{iz} = \sqrt{\beta^2 n_m^2 - k_{ix}^2 - k_{iy}^2}$. Equation (4.17) becomes:

$$\left(\tilde{\chi}_{xx} - \tilde{\chi}_{xy}\right)(k_x - k_{ix}, k_y - k_{iy}, q - k_{iz}) = \frac{i\sqrt{2}\pi q}{\beta^2}\tilde{U}_{sx2}(k_x, k_y; z = 0);$$

$$\left(\tilde{\chi}_{yx} - \tilde{\chi}_{yy}\right)(k_x - k_{ix}, k_y - k_{iy}, q - k_{iz}) = \frac{i\sqrt{2}\pi q}{\beta^2}\tilde{U}_{sy2}(k_x, k_y; z = 0). \tag{4.21}$$

Shifting the illumination angle repeatedly, we will be able to reconstructed the three- dimensional structures. Eqns. (4.18)-(4.20) can still be used here to retrieve the three-dimension birefringence and orientation angle distribution.Here we assume the birefringent sample has layer structures (stacked by 2D birefringent structures), in the future we want to extend this theory into more general case.

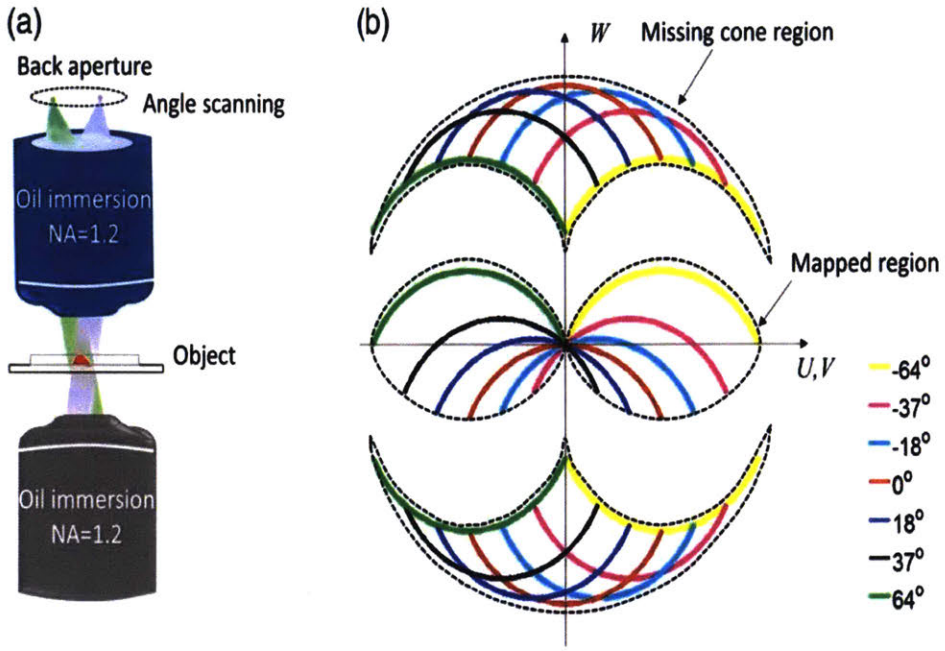

Figure 4-1: Illustration of angle scanning-based scattered field measurements and frequency domain mapping.

4.5 Possible System Design

In this part, I propose a possible system design for anisotropic optical diffraction microscopy, which is shown in figure 4.2. This system is very similar to the conventional optical diffraction tomography setup, however, I used two linear polarizers before and after the sample to adjust the illumination and detection polarization state. In this way, we will be able to realize the three-dimensional reconstruction of the polarization parameter distributions (birefringence and orientation angle).

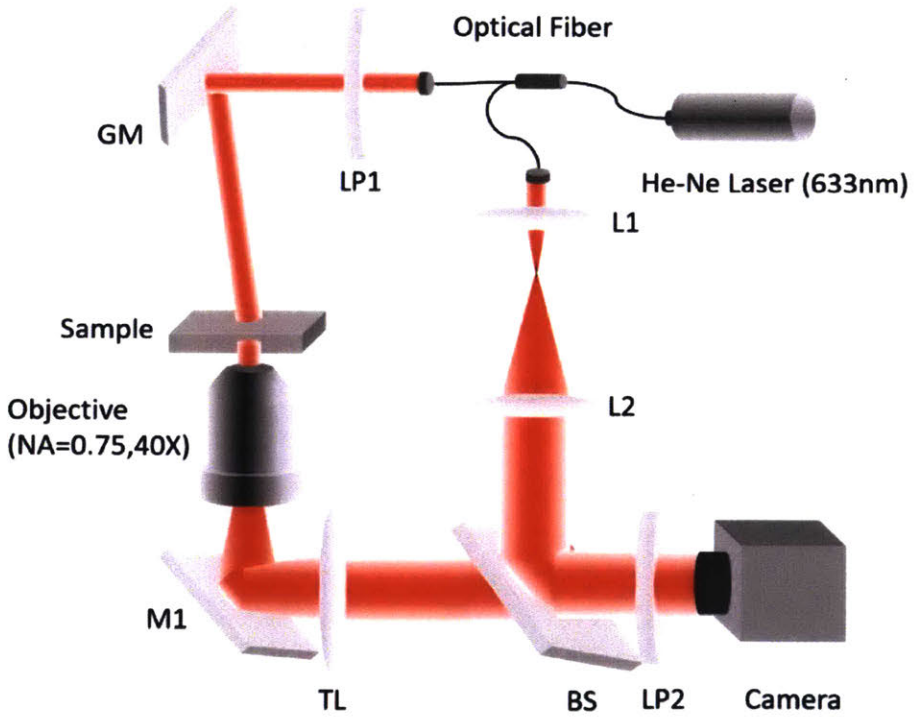

Figure 4-2: Possible system design for anisotropic optical diffraction tomography. GM, galvo scanner; TL, tube lens; LP1, LP2, linear polarizers; M1, mirror; BS, beam splitter.

Chapter 5

Future Work

In this thesis, I introduced most of my work about developing novel optical imaging techniques when I am finishing my master degree. In the future, during my doctoral years, one of my major goal is to apply these novel techniques to biological and nano-material researches, for solving important scientific problems or satisfying industrial needs. In the chapter, I will list some of these potential applications.

5.1 Sickle Cell Anemia(SCA)

Sickle cell anemia (SCA) is a worldwide autosomal recessive disease[80]. In SCA, a point mutation occurs in the gene responsible for the production of β-chain in hemoglobin (Hb), resulting in the rise to hemoglobin S (HbS), a variant form of Hb[81, 82]. Under low-oxygen (hypoxic) conditions, the hydrophobic residues within cytosol associate with one another to form polymerized fibers that alter the RBC shape[83]. This process has been well studied over the recent several decades. However, it remains unclear that how the polymerization process occurs during the oxy-deoxy transient change. The birefringence of the polymerized HbS is an intrinsic marker for this polymerization process[84]. Therefore, polarization microscopy with high sensitivity and high imaging speed, such as high sensitivity retardance imaging and QPIM I mentioned before, will be a proper technique for the study of HbS polymerization dynamics[85].

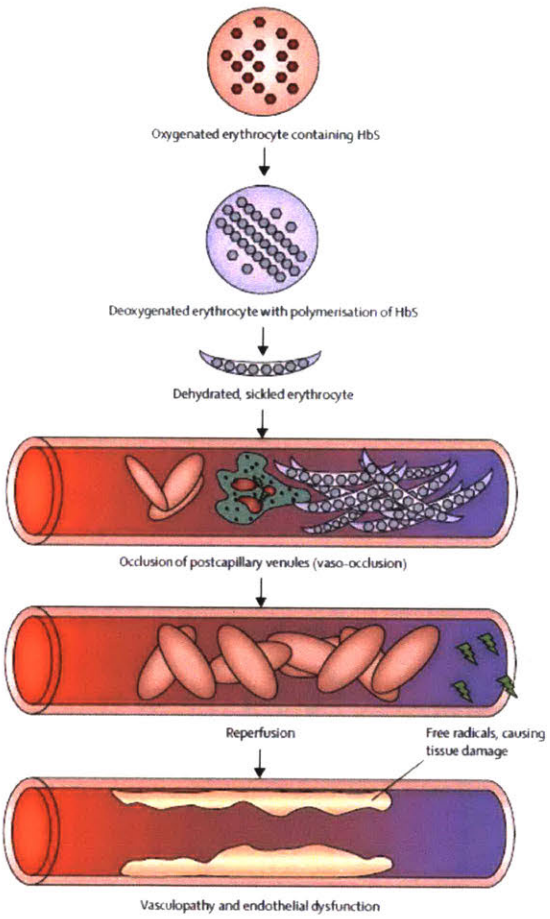

Figure 5-1: Pathophysiology of sickle-cell disease.

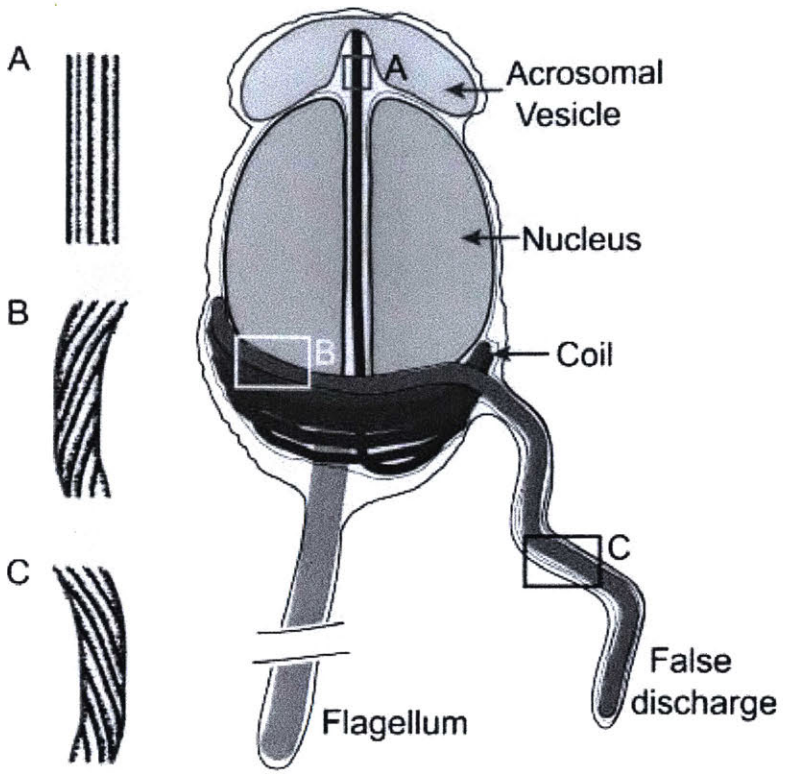

Figure 5-2: A schematic of Limulus sperm based on electron micrographs. The filaments are twisted in the coiled state and the FD state with opposite chirality but straight in the TD state. During the acrosomal reaction, the actin filaments untwist and unbend going from the coil to the TD. Sometimes the unbending does not occur, leading to kinked TDs

5.2 The acrosome reaction of crab sperms

The acrosome reaction of the sperm of the horseshoe crab Limulus Polyphemus is an unusual example of actin-based motility. Upon contact with the egg jelly coat, a bundle of actin filaments cross-linked by $scruin-CaM$ heterodimers extends from the head of the sperm through a nuclear channel to form a 60-μm-long finger of membrane, the acrosomal process. Since the bundled actin filaments are highly anisotropic, the quantitative polarization imaging will help the biologists to quantify the acrosome process[77–79]. Our QPIM system has the potential to quantitatively image the optical anisotropy in a single-shot, which will be quite helpful for the study of the discharging dynamics[86].

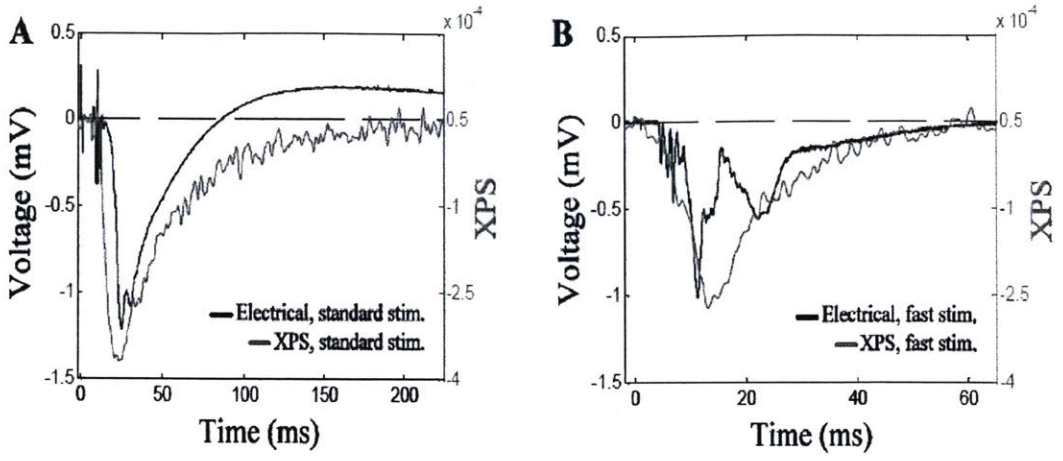

Figure 5-3: A) The electrical recording (black) and XPS (red) at a standard stimulation rate, 2 Hz. The nerve demonstrates an adaptive response to the faster stimulus, and no reversal of polarity, which is evident with a standard stimulation rate. B) The electrical recording (black) and XPS (red) at a faster stimulation rate, 14 Hz. The XPS peak width is reduced with a faster stimulation, which may indicate a reduction in the recruitment of axons to generate action potentials as a result of adaptation to fast stimulation. The peak of the XPS coincides with the peak of the electrical recording for both fast and standard stimulation rates.

5.3 Label-free imaging of neuron action potential

The cytoskeleton forms the basis of neuronal polarity and directs intracellular trafficking, and filament actin and microtubules are two major cytoskeleton elements of cytoskeletons[24]. F-actin is not responsible for long-distance transport along dendritic or axonal processes. Microtubules fill the center of the axonal and dendritic processes, and therefore are the cytoskeletal element along which long-distance transport in neuronal process occurs. During the process of action potential propagation, the birefringence of the axon will change at an extent of 1×10^{-4}. This is perhaps the intrinsic marker for the action potential process[87]. Recently, most of the action potential imaging is based on fluorescence. The labeling is laborious and may cause the perturbation of the living process of the neuron cells. Therefore, birefringence imaging for neuron activity may be a promising field and a great alternative imaging method[88, 89].

5.4 Semiconductor wafer inspection

The fabrication defects on wafers often lead to short circuit or disconnection, which can severely degrade the performance of chips[90–92]. Therefore, defect inspection is always significant in the process of semiconductor fabrication. Recent advances in multiple patterning ultra-violet (UV) lithography and extreme-UV (EUV) lithography enables fabricated wafers with node size below 10 nm[93, 94]. To spot the defects on the semiconductor wafer with such small node size, techniques based on electron-beam (e-beam) scanning, such as SEM, TEM are reported to be used for wafer inspection[95–97]. Although these techniques can often achieve nanoscale resolution, the efficiency and cost are inevitably sacrificed[98–101]. For example, a typical SEM can resolve nanoscale structures down to the size of nearly 10 nm. However, the image field of SEM has to be shrunk to about $1\mu m \times 1\mu m$ to reach such high resolution (with a pixel size about 1 nm accordingly), which means it will take over a month to scan only one 5-inch wafer[102]. Multiple electron beams (more than 100) were proposed to boost the efficiency, but the detection cost per area with this method increased dramatically[103, 104]. Similar problems occur when using TEM. SAXS is a promising technology because this technique enables the entire three-dimensional imaging of IC with very high resolution ($\sim$ 14 nm)[105]. Unfortunately, the necessity to use synchrotron light sources limits its broad application. The existence of the defect on the semiconductor wafer will break the uniformity on the surface, which will introduce the optical anisotropy. Therefore, polarization microscopy with high sensitivity will have a great potential to find nanoscale defects on the wafer. Furthermore, high sensitivity polarization microscopes in reflection mode also has the potential to be applied to the inspection of other materials.

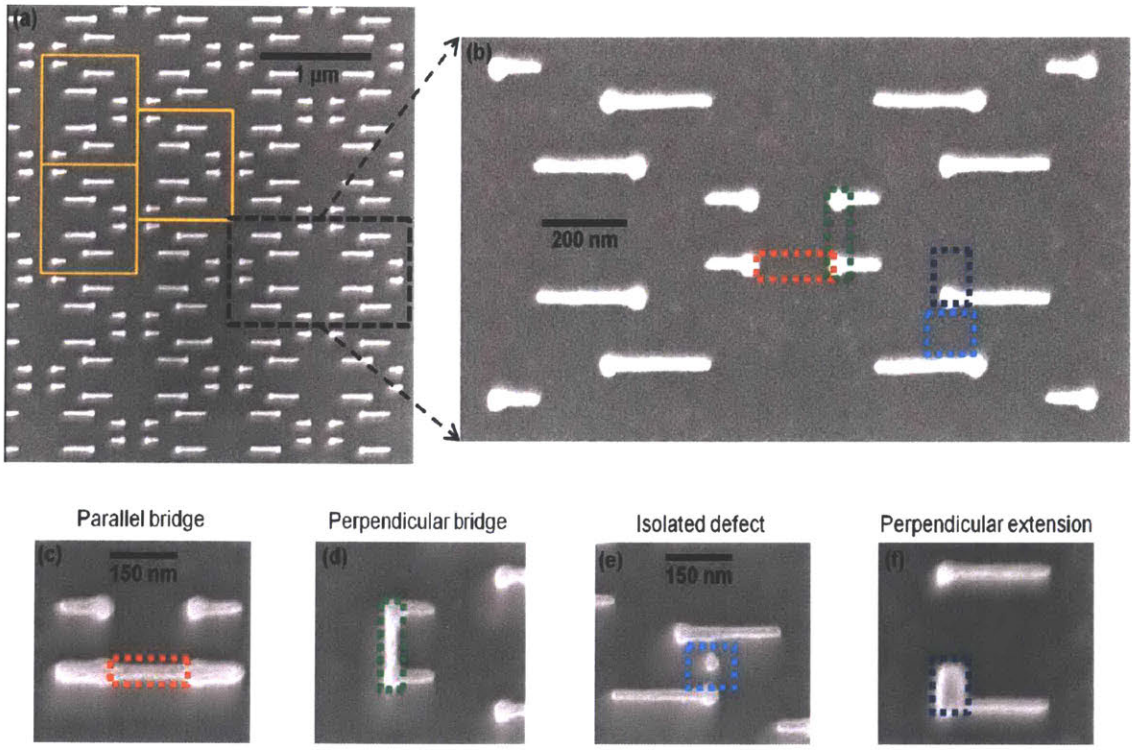

Figure 5-4: SEM images illustrate the printed defects in the large area nanopatterned structure. (a) A defect free portion of the pattern, showing the unit cell in orange. (b) A zoomed-in portion of the pattern, where the locations of the four different type of defects are marked by colored boxes. (c) A parallel bridge defect (red). (d) A perpendicular bridge defect (green). (e) An isolated dot defect (light-blue). (f) A perpendicular line extension defect (dark-blue).

Bibliography

[1] Walter C McCrone, Lucy B McCrone, and John Gustav Delly. *Polarized light microscopy.* Ann Arbor Science Publishers Inc. and McCrone Research Institute, 1978.

[2] Eugene Fredericq and Claude Houssier. Electric dichroism and electric birefringence. 1973.

[3] Pochi Yeh and Claire Gu. *Optics of Liquid Crystal Displays*, volume 67. John Wiley & Sons, 2010.

[4] Carsten Benecke, Hubert Seiberle, and Martin Schadt. Determination of director distributions in liquid crystal polymer-films by means of generalized anisotropic ellipsometry. *Japanese Journal of Applied Physics*, 39(2R):525, 2000.

[5] Ichiro Hirosawa. Method of characterizing rubbed polyimide film for liquid crystal display devices using reflection ellipsometry. *Japanese Journal of Applied Physics*, 35(11R):5873, 1996.

[6] Mathias Schubert, Bernd Rheinländer, Christiane Cramer, Herbert Schmiedel, John A Woollam, Craig M Herzinger, and Blaine Johs. Generalized transmission ellipsometry for twisted biaxial dielectric media: application to chiral liquid crystals. *JOSA A*, 13(9):1930–1940, 1996.

[7] Kostya S Novoselov, Andre K Geim, Sergei V Morozov, D Jiang, Y_ Zhang,

Sergey V Dubonos, Irina V Grigorieva, and Alexandr A Firsov. Electric field effect in atomically thin carbon films. *Science*, 306(5696):666–669, 2004.

[8] Han Liu, Adam T Neal, Zhen Zhu, Zhe Luo, Xianfan Xu, David Tománek, and Peide D Ye. Phosphorene: an unexplored 2d semiconductor with a high hole mobility. *ACS nano*, 8(4):4033–4041, 2014.

[9] Han Liu, Yuchen Du, Yexin Deng, and D Ye Peide. Semiconducting black phosphorus: synthesis, transport properties and electronic applications. *Chemical Society Reviews*, 44(9):2732–2743, 2015.

[10] Yexin Deng, Zhe Luo, Nathan J Conrad, Han Liu, Yongji Gong, Sina Najmaei, Pulickel M Ajayan, Jun Lou, Xianfan Xu, and Peide D Ye. Black phosphorus–monolayer mos2 van der waals heterojunction p–n diode. *ACS nano*, 8(8):8292–8299, 2014.

[11] OA Balitskii, B Jaeckel, and W Jaegermann. Surface properties of gate single crystals. *Physics Letters A*, 372(18):3303–3306, 2008.

[12] Shengxi Huang, Yuki Tatsumi, Xi Ling, Huaihong Guo, Ziqiang Wang, Garrett Watson, Alexander A Puretzky, David B Geohegan, Jing Kong, Ju Li, et al. In-plane optical anisotropy of layered gallium telluride. *ACS nano*, 10(9):8964–8972, 2016.

[13] Xi Ling, Shengxi Huang, Eddwi H Hasdeo, Liangbo Liang, William M Parkin, Yuki Tatsumi, Ahmad RT Nugraha, Alexander A Puretzky, Paul Masih Das, Bobby G Sumpter, et al. Anisotropic electron-photon and electron-phonon interactions in black phosphorus. *Nano Letters*, 16(4):2260–2267, 2016.

[14] Jingsi Qiao, Xianghua Kong, Zhi-Xin Hu, Feng Yang, and Wei Ji. High-mobility transport anisotropy and linear dichroism in few-layer black phosphorus. *Nature Communications*, 5:4475, 2014.

[15] José F Rodríguez, Cristina Ruiz, Manuel Doblaré, and Gerhard A Holzapfel. Mechanical stresses in abdominal aortic aneurysms: influence of diameter,

asymmetry, and material anisotropy. *Journal of Biomechanical Engineering*, 130(2):021023, 2008.

[16] Trushant S Majmudar and Robert P Behringer. Contact force measurements and stress-induced anisotropy in granular materials. *Nature*, 435(7045):1079, 2005.

[17] Arend M Van Der Zande, Pinshane Y Huang, Daniel A Chenet, Timothy C Berkelbach, YuMeng You, Gwan-Hyoung Lee, Tony F Heinz, David R Reichman, David A Muller, and James C Hone. Grains and grain boundaries in highly crystalline monolayer molybdenum disulphide. *Nature Materials*, 12(6):554, 2013.

[18] Andrzej L Bajor. Automated polarimeter–macroscope for optical mapping of birefringence, azimuths, and transmission in large area wafers. part i. theory of the measurement. *Review of Scientific Instruments*, 66(4):2977–2990, 1995.

[19] Il-Buem Lee, Hyeon-Min Moon, Jong-Hyeon Joo, Kyoung-Hoon Kim, Seok-Cheol Hong, and Minhaeng Cho. Interferometric scattering microscopy with polarization-selective dual detection scheme: Capturing the orientational information of anisotropic nanometric objects. *ACS Photonics*, 2017.

[20] R Oldenbourg, ED Salmon, and PT Tran. Birefringence of single and bundled microtubules. *Biophysical Journal*, 74(1):645–654, 1998.

[21] Harvey Lodish, Arnold Berk, S Lawrence Zipursky, Paul Matsudaira, David Baltimore, James Darnell, et al. *Molecular cell biology*, volume 3. WH Freeman New York, 1995.

[22] Benjamin Geiger, Alexander Bershadsky, Roumen Pankov, and Kenneth M Yamada. Transmembrane crosstalk between the extracellular matrix and the cytoskeleton. *Nature Reviews Molecular Cell Biology*, 2(11):793, 2001.

[23] Anne J Ridley, Martin A Schwartz, Keith Burridge, Richard A Firtel, Mark H Ginsberg, Gary Borisy, J Thomas Parsons, and Alan Rick Horwitz. Cell mi-

gration: integrating signals from front to back. *Science*, 302(5651):1704–1709, 2003.

[24] Liqun Luo. *Principles of neurobiology*. Garland Science, 2015.

[25] Rebecca M Williams, Warren R Zipfel, and Watt W Webb. Interpreting second-harmonic generation images of collagen i fibrils. *Biophysical Journal*, 88(2):1377–1386, 2005.

[26] Nirmal Mazumder, Gitanjal Deka, Wei-Wen Wu, Ankur Gogoi, Guan-Yu Zhuo, and Fu-Jen Kao. Polarization resolved second harmonic microscopy. *Methods*, 128:105–118, 2017.

[27] Jeff W Lichtman and José-Angel Conchello. Fluorescence microscopy. *Nature methods*, 2(12):910, 2005.

[28] Shalin B Mehta, Molly McQuilken, Patrick J La Riviere, Patricia Occhipinti, Amitabh Verma, Rudolf Oldenbourg, Amy S Gladfelter, and Tomomi Tani. Dissection of molecular assembly dynamics by tracking orientation and position of single molecules in live cells. *Proceedings of the National Academy of Sciences*, 113(42):E6352–E6361, 2016.

[29] Daniel Axelrod. Fluorescence polarization microscopy. In *Methods in Cell Biology*, volume 30, pages 333–352. Elsevier, 1989.

[30] Cesar Augusto Valades Cruz, Haitham Ahmed Shaban, Alla Kress, Nicolas Bertaux, Serge Monneret, Manos Mavrakis, Julien Savatier, and Sophie Brasselet. Quantitative nanoscale imaging of orientational order in biological filaments by polarized superresolution microscopy. *Proceedings of the National Academy of Sciences*, 113(7):E820–E828, 2016.

[31] William A Shurcliff. Polarized light. production and use. *Cambridge, Mass.: Harvard University Press,/ c1966*, 1966.

[32] Emil Wolf. Unified theory of coherence and polarization of random electromagnetic beams. *Physics Letters A*, 312(5-6):263–267, 2003.

[33] Rudolf Oldenbourg. A new view on polarization microscopy. *Nature*, 381(6585):811, 1996.

[34] R Oldenbourg and G Mei. New polarized light microscope with precision universal compensator. *Journal of Microscopy*, 180(2):140–147, 1995.

[35] Michael Shribak and Rudolf Oldenbourg. Techniques for fast and sensitive measurements of two-dimensional birefringence distributions. *Applied Optics*, 42(16):3009–3017, 2003.

[36] Kaoru Katoh, Katherine Hammar, Peter JS Smith, and Rudolf Oldenbourg. Birefringence imaging directly reveals architectural dynamics of filamentous actin in living growth cones. *Molecular Biology of the Cell*, 10(1):197–210, 1999.

[37] David Huang, Eric A Swanson, Charles P Lin, Joel S Schuman, William G Stinson, Warren Chang, Michael R Hee, Thomas Flotte, Kenton Gregory, Carmen A Puliafito, et al. Optical coherence tomography. *Science*, 254(5035):1178–1181, 1991.

[38] Michael R Hee, Joseph A Izatt, Eric A Swanson, David Huang, Joel S Schuman, Charles P Lin, Carmen A Puliafito, and James G Fujimoto. Optical coherence tomography of the human retina. *Archives of Ophthalmology*, 113(3):325–332, 1995.

[39] Wolfgang Drexler, Uwe Morgner, Ravi K Ghanta, Franz X Kärtner, Joel S Schuman, and James G Fujimoto. Ultrahigh-resolution ophthalmic optical coherence tomography. *Nature Medicine*, 7(4):502, 2001.

[40] Joseph A Izatt, Manish D Kulkarni, Siavash Yazdanfar, Jennifer K Barton, and Ashley J Welch. In vivo bidirectional color doppler flow imaging of picoliter

blood volumes using optical coherence tomography. *Optics Letters*, 22(18):1439–1441, 1997.

[41] Yonghua Zhao, Zhongping Chen, Christopher Saxer, Shaohua Xiang, Johannes F de Boer, and J Stuart Nelson. Phase-resolved optical coherence tomography and optical doppler tomography for imaging blood flow in human skin with fast scanning speed and high velocity sensitivity. *Optics Letters*, 25(2):114–116, 2000.

[42] Johannes F De Boer, Thomas E Milner, Martin JC van Gemert, and J Stuart Nelson. Two-dimensional birefringence imaging in biological tissue by polarization-sensitive optical coherence tomography. *Optics Letters*, 22(12):934–936, 1997.

[43] Johannes F De Boer, Thomas E Milner, and J Stuart Nelson. Determination of the depth-resolved stokes parameters of light backscattered from turbid media by use of polarization-sensitive optical coherence tomography. *Optics Letters*, 24(5):300–302, 1999.

[44] Johannes F De Boer, Christoph K Hitzenberger, and Yoshiaki Yasuno. Polarization sensitive optical coherence tomography–a review. *Biomedical Optics Express*, 8(3):1838–1873, 2017.

[45] Michael J Pelletier. *Analytical applications of Raman spectroscopy.* Wiley-Blackwell, 1999.

[46] GS Duesberg, I Loa, M Burghard, K Syassen, and S Roth. Polarized raman spectroscopy on isolated single-wall carbon nanotubes. *Physical Review Letters*, 85(25):5436, 2000.

[47] Tingkui Mu, Chunmin Zhang, and Rongguang Liang. Demonstration of a snapshot full-stokes division-of-aperture imaging polarimeter using wollaston prism array. *Journal of Optics*, 17(12):125708, 2015.

[48] Gabriel Popescu. *Quantitative phase imaging of cells and tissues.* McGraw Hill Professional, 2011.

[49] Samira Khadir, Pierre Bon, Dominique Vignaud, Elizabeth Galopin, Niall McEvoy, David McCloskey, Serge Monneret, and Guillaume Baffou. Optical imaging and characterization of graphene and other 2d materials using quantitative phase microscopy. *ACS photonics*, 4(12):3130–3139, 2017.

[50] Zhuo Wang, Larry J Millet, Martha U Gillette, and Gabriel Popescu. Jones phase microscopy of transparent and anisotropic samples. *Optics Letters*, 33(11):1270–1272, 2008.

[51] Youngchan Kim, Joonwoo Jeong, Jaeduck Jang, Mahn Won Kim, and YongKeun Park. Polarization holographic microscopy for extracting spatio-temporally resolved jones matrix. *Optics Express*, 20(9):9948–9955, 2012.

[52] Sherazade Aknoun, Pierre Bon, Julien Savatier, Benoit Wattellier, and Serge Monneret. Quantitative retardance imaging of biological samples using quadri-wave lateral shearing interferometry. *Optics Express*, 23(12):16383–16406, 2015.

[53] Chengshuai Li, Shichao Chen, Michael Klemba, and Yizheng Zhu. Integrated quantitative phase and birefringence microscopy for imaging malaria-infected red blood cells. *Journal of Biomedical Optics*, 21(9):090501, 2016.

[54] Wonshik Choi, Christopher Fang-Yen, Kamran Badizadegan, Seungeun Oh, Niyom Lue, Ramachandra R Dasari, and Michael S Feld. Tomographic phase microscopy. *Nature Methods*, 4(9):717, 2007.

[55] Yongjin Sung, Wonshik Choi, Christopher Fang-Yen, Kamran Badizadegan, Ramachandra R Dasari, and Michael S Feld. Optical diffraction tomography for high resolution live cell imaging. *Optics Express*, 17(1):266–277, 2009.

[56] Vincent Lauer. New approach to optical diffraction tomography yielding a vector equation of diffraction tomography and a novel tomographic microscope. *Journal of Microscopy*, 205(2):165–176, 2002.

[57] Kyoohyun Kim, Kyung Sang Kim, HyunJoo Park, Jong Chul Ye, and YongKeun Park. Real-time visualization of 3-d dynamic microscopic objects using optical diffraction tomography. *Optics Express*, 21(26):32269–32278, 2013.

[58] JooWon Lim, KyeoReh Lee, Kyong Hwan Jin, Seungwoo Shin, SeoEun Lee, YongKeun Park, and Jong Chul Ye. Comparative study of iterative reconstruction algorithms for missing cone problems in optical diffraction tomography. *Optics Express*, 23(13):16933–16948, 2015.

[59] Taewoo Kim, Renjie Zhou, Mustafa Mir, S Derin Babacan, P Scott Carney, Lynford L Goddard, and Gabriel Popescu. White-light diffraction tomography of unlabelled live cells. *Nature Photonics*, 8(3):256, 2014.

[60] CR Burch and JPP Stock. Phase-contrast microscopy. *Journal of Scientific Instruments*, 19(5):71, 1942.

[61] Pierre Marquet, Benjamin Rappaz, Pierre J Magistretti, Etienne Cuche, Yves Emery, Tristan Colomb, and Christian Depeursinge. Digital holographic microscopy: a noninvasive contrast imaging technique allowing quantitative visualization of living cells with subwavelength axial accuracy. *Optics Letters*, 30(5):468–470, 2005.

[62] Jian Sheng, Edwin Malkiel, and Joseph Katz. Digital holographic microscope for measuring three-dimensional particle distributions and motions. *Applied Optics*, 45(16):3893–3901, 2006.

[63] Jonas Kühn, Tristan Colomb, Frédéric Montfort, Florian Charrière, Yves Emery, Etienne Cuche, Pierre Marquet, and Christian Depeursinge. Real-time dual-wavelength digital holographic microscopy with a single hologram acquisition. *Optics Express*, 15(12):7231–7242, 2007.

[64] Gabriel Popescu, Lauren P Deflores, Joshua C Vaughan, Kamran Badizadegan, Hidenao Iwai, Ramachandra R Dasari, and Michael S Feld. Fourier phase mi-

croscopy for investigation of biological structures and dynamics. *Optics Letters*, 29(21):2503–2505, 2004.

[65] Richard M Goldstein, Howard A Zebker, and Charles L Werner. Satellite radar interferometry: Two-dimensional phase unwrapping. *Radio Science*, 23(4):713–720, 1988.

[66] Gabriel Popescu, Takahiro Ikeda, Ramachandra R Dasari, and Michael S Feld. Diffraction phase microscopy for quantifying cell structure and dynamics. *Optics Letters*, 31(6):775–777, 2006.

[67] Basanta Bhaduri, Hoa Pham, Mustafa Mir, and Gabriel Popescu. Diffraction phase microscopy with white light. *Optics Letters*, 37(6):1094–1096, 2012.

[68] YongKeun Park, Gabriel Popescu, Takahiro Ikeda, Kamran Badizadegan, Ramachandra R Dasari, and Michael S Feld. Diffraction phase microscopy. In *Biomedical Topical Meeting*, page TuI50. Optical Society of America, 2006.

[69] Basanta Bhaduri, Chris Edwards, Hoa Pham, Renjie Zhou, Tan H Nguyen, Lynford L Goddard, and Gabriel Popescu. Diffraction phase microscopy: principles and applications in materials and life sciences. *Advances in Optics and Photonics*, 6(1):57–119, 2014.

[70] Mohammad Reza Jafarfard, Sucbei Moon, Behnam Tayebi, and Dug Young Kim. Dual-wavelength diffraction phase microscopy for simultaneous measurement of refractive index and thickness. *Optics Letters*, 39(10):2908–2911, 2014.

[71] Zhuo Wang, Larry Millet, Mustafa Mir, Huafeng Ding, Sakulsuk Unarunotai, John Rogers, Martha U Gillette, and Gabriel Popescu. Spatial light interference microscopy (slim). *Optics Express*, 19(2):1016–1026, 2011.

[72] Zhuo Wang, Huafeng Ding, Rashid Bashir, Gabriel Popescu, Larry Millet, Martha Gillette, and Vincent Chan. Label-free intracellular transport measured by spatial light interference microscopy. *Journal of Biomedical Optics*, 16(2):026019, 2011.

[73] S Derin Babacan, Zhuo Wang, Minh Do, and Gabriel Popescu. Cell imaging beyond the diffraction limit using sparse deconvolution spatial light interference microscopy. *Biomedical Optics Express*, 2(7):1815–1827, 2011.

[74] Di Jin, Renjie Zhou, Zahid Yaqoob, and Peter TC So. Tomographic phase microscopy: principles and applications in bioimaging. *JOSA B*, 34(5):B64–B77, 2017.

[75] Poorya Hosseini, Renjie Zhou, Yang-Hyo Kim, Chiara Peres, Alberto Diaspro, Cuifang Kuang, Zahid Yaqoob, and Peter TC So. Pushing phase and amplitude sensitivity limits in interferometric microscopy. *Optics Letters*, 41(7):1656–1659, 2016.

[76] AA Chabanov, M Stoytchev, and AZ Genack. Statistical signatures of photon localization. *Nature*, 404(6780):850, 2000.

[77] Jennifer H Shin, L Mahadevan, Guillermina S Waller, Knut Langsetmo, and Paul Matsudaira. Stored elastic energy powers the 60-μm extension of the limulus polyphemus sperm actin bundle. *The Journal of cell biology*, 162(7):1183–1188, 2003.

[78] David J DeRosier, Lewis G Tilney, Edward M Bonder, and Phyllis Frankl. A change in twist of actin provides the force for the extension of the acrosomal process in limulus sperm: the false-discharge reaction. *The Journal of cell biology*, 93(2):324, 1982.

[79] Lewis G Tilney. Actin filaments in the acrosomal reaction of limulus sperm. motion generated by alterations in the packing of the filaments. *The Journal of Cell Biology*, 64(2):289–310, 1975.

[80] II Abubakar, T Tillmann, and A Banerjee. Global, regional, and national age-sex specific all-cause and cause-specific mortality for 240 causes of death, 1990-2013: a systematic analysis for the global burden of disease study 2013. *Lancet*, 385(9963):117–171, 2015.

[81] Vernon M Ingram et al. Gene mutations in human haemoglobin: the chemical difference between normal and sickle cell haemoglobin. *Nature*, 180(4581):326–328, 1957.

[82] William A Eaton and James Hofrichter. The biophysics of sickle cell hydroxyurea therapy. *Science*, 268(5214):1142, 1995.

[83] William A Eaton and James Hofrichter. Sickle cell hemoglobin polymerization. In *Advances in protein chemistry*, volume 40, pages 63–279. Elsevier, 1990.

[84] Garrott W Christoph, James Hofrichter, and William A Eaton. Understanding the shape of sickled red cells. *Biophysical journal*, 88(2):1371–1376, 2005.

[85] Poorya Hosseini, Sabia Z Abidi, E Du, Dimitrios P Papageorgiou, Youngwoon Choi, YongKeun Park, John M Higgins, Gregory J Kato, Subra Suresh, Ming Dao, et al. Cellular normoxic biophysical markers of hydroxyurea treatment in sickle cell disease. *Proceedings of the National Academy of Sciences*, 113(34):9527–9532, 2016.

[86] Kaoru Katoh, Katsuyiki Yamada, Fumio Oosawa, and Rudolf Oldenbourg. Birefringence measurements of the actin bundle in the acrosomal processes of limulus sperm. *The Biological Bulletin*, 191(2):270–271, 1996.

[87] LB Cohen, RD Keynes, and Bertil Hille. Light scattering and birefringence changes during nerve activity. *Nature*, 218(5140):438, 1968.

[88] Ali H Badreddine, Tomas Jordan, and Irving J Bigio. Real-time imaging of action potentials in nerves using changes in birefringence. *Biomedical Optics Express*, 7(5):1966–1973, 2016.

[89] Subrata Batabyal, Sarmishtha Satpathy, Loan Bui, Young-Tae Kim, Samarendra Mohanty, Robert Bachoo, and Digant P Davé. Label-free optical detection of action potential in mammalian neurons. *Biomedical Optics Express*, 8(8):3700–3713, 2017.

[90] Jer-Shing Huang, Victor Callegari, Peter Geisler, Christoph Brüning, Johannes Kern, Jord C Prangsma, Xiaofei Wu, Thorsten Feichtner, Johannes Ziegler, Pia Weinmann, et al. Atomically flat single-crystalline gold nanostructures for plasmonic nanocircuitry. *Nature Communications*, 1:150, 2010.

[91] Martin Kalbac, Ya-Ping Hsieh, Hootan Farhat, Ladislav Kavan, Mario Hofmann, Jing Kong, and Mildred S Dresselhaus. Defects in individual semiconducting single wall carbon nanotubes: Raman spectroscopic and in situ raman spectroelectrochemical study. *Nano Letters*, 10(11):4619–4626, 2010.

[92] Koki Urita, Yuta Sato, Kazu Suenaga, Alexandre Gloter, Ayako Hashimoto, Masashi Ishida, Takashi Shimada, Hisanori Shinohara, and Sumio Iijima. Defect-induced atomic migration in carbon nanopeapod: tracking the single-atom dynamic behavior. *Nano Letters*, 4(12):2451–2454, 2004.

[93] Bryan M Barnes, Martin Y Sohn, Francois Goasmat, Hui Zhou, András E Vladár, Richard M Silver, and Abraham Arceo. Three-dimensional deep sub-wavelength defect detection using λ= 193 nm optical microscopy. *Optics Express*, 21(22):26219–26226, 2013.

[94] Matthew D Seaberg, Bosheng Zhang, Dennis F Gardner, Elisabeth R Shanblatt, Margaret M Murnane, Henry C Kapteyn, and Daniel E Adams. Tabletop nanometer extreme ultraviolet imaging in an extended reflection mode using coherent fresnel ptychography. *Optica*, 1(1):39–44, 2014.

[95] Joseph I Goldstein, Dale E Newbury, Joseph R Michael, Nicholas WM Ritchie, John Henry J Scott, and David C Joy. *Scanning electron microscopy and X-ray microanalysis*. Springer, 2017.

[96] David B Williams and C Barry Carter. The transmission electron microscope. In *Transmission electron microscopy*, pages 3–17. Springer, 1996.

[97] HJ Leamy. Charge collection scanning electron microscopy. *Journal of Applied Physics*, 53(6):R51–R80, 1982.

[98] Renjie Zhou, Chris Edwards, Amir Arbabi, Gabriel Popescu, and Lynford L Goddard. Detecting 20 nm wide defects in large area nanopatterns using optical interferometric microscopy. *Nano Letters*, 13(8):3716–3721, 2013.

[99] Takanori Kudo, Jun-Bom Bae, Ralph R Dammel, Woo-Kyu Kim, Douglas S McKenzie, M Dalil Rahman, Munirathna Padmanaban, and Waiman Ng. Cd changes of 193-nm resists during sem measurement. In *Advances in Resist Technology and Processing XVIII*, volume 4345, pages 179–190. International Society for Optics and Photonics, 2001.

[100] RF Egerton, P Li, and M Malac. Radiation damage in the tem and sem. *Micron*, 35(6):399–409, 2004.

[101] Cattien V Nguyen, Ramsey MD Stevens, Jabulani Barber, Jie Han, M Meyyappan, Martha I Sanchez, Carl Larson, and William D Hinsberg. Carbon nanotube scanning probe for profiling of deep-ultraviolet and 193 nm photoresist patterns. *Applied Physics Letters*, 81(5):901–903, 2002.

[102] Richard F Hafer, Oliver D Patterson, Roland Hahn, and Hong Xiao. Full-wafer electron beam inspection for detection of beol defects. In *Advanced Semiconductor Manufacturing Conference (ASMC), 2014 25th Annual SEMI*, pages 397–404. IEEE, 2014.

[103] Brad Thiel, Maseeh Mukhtar, Kathy Quoi, Benjamin D Bunday, and Matt Malloy. Patterned wafer inspection with multi-beam sem technology. *Microscopy and Microanalysis*, 22:586, 2016.

[104] Brad Thiel, Michael Lercel, Benjamin Bunday, and Matt Malloy. Assessing the viability of multi-electron beam wafer inspection for sub-20nm defects. In *Scanning Microscopies 2014*, volume 9236, page 92360E. International Society for Optics and Photonics, 2014.

[105] Mirko Holler, Manuel Guizar-Sicairos, Esther HR Tsai, Roberto Dinapoli, Elisabeth Müller, Oliver Bunk, Jörg Raabe, and Gabriel Aeppli. High-

resolution non-destructive three-dimensional imaging of integrated circuits. *Nature*, 543(7645):402, 2017.